J. Fluid Mech. (1997), *vol.* 353, *pp.* 1–30. Printed in the United Kingdom

Dynamic simulation of shear thickening in concentrated colloidal suspensions

By D. I. DRATLER[1]† W. R. SCHOWALTER[1] AND R. L. HOFFMAN[2]

[1] Department of Chemical Engineering, University of Illinois, Urbana, IL 61801, USA

[2] Polymer Research Group, Department of Chemical Engineering, University of New Hampshire, Durham, NH 03824, USA

(Received 23 July 1996 and in revised form 19 June 1997)

Stokesian Dynamics has been used to investigate the origins of shear thickening in concentrated colloidal suspensions. For this study, we considered a monolayer suspension composed of charge-stabilized non-Brownian monosized rigid spheres dispersed at an areal fraction of $\phi_a = 0.74$ in a Newtonian liquid. The suspension was subjected to a linear shear field. In agreement with established experimental data, our results indicate that shear thickening in this system is associated with an order–disorder transition of the suspension microstructure. Below the critical shear rate at which this transition occurs, the suspension microstructure consists of two-dimensional analogues of experimentally observed sliding layer configurations. Above this critical shear rate, suspensions are disordered, contain particle clusters, and exhibit viscosities and microstructures characteristic of suspensions of non-Brownian hard spheres. In addition, suspensions possessing the sliding layer microstructure at the beginning of supercritical shearing tend to retain this microstructure for a period of time before disordering. The onset of this disorder is due to the formation of particle doublets within the suspension. Once formed, these doublets rotate, due to the bulk motion, and disrupt the long-range order of the suspension. The cross-stream component of the centre-to-centre separation vector associated with the two particles forming a doublet, which is zero when the doublet is perfectly aligned with the bulk velocity vector, grows exponentially with time. This strongly suggests that the evolution of these doublets is due to a change in the stability of the sliding layer configurations, with this type of ordered microstructure being linearly unstable above a critical shear rate. This contention is supported by results of a stability analysis. The analysis shows that a single string of particles is subject to a linear instability leading to the formation of particle doublets. Simulations were repeated with different numbers of particles in the computational domain, with the results found to be qualitatively independent of system size.

1. Introduction

In spite of the importance of colloidal suspensions in commercial applications, the phenomenon of shear thickening in these materials remains poorly understood. Shear thickening, which can adversely affect many types of industrial processes (see Barnes 1989), is quite common and has been observed in hard-sphere systems (see e.g. Bender & Wagner 1996), mono- and polydisperse suspensions of repulsive particles (see e.g.

† Present address: Exxon Production Research Company, PO Box 2189, Houston, TX 77252-2189, USA.

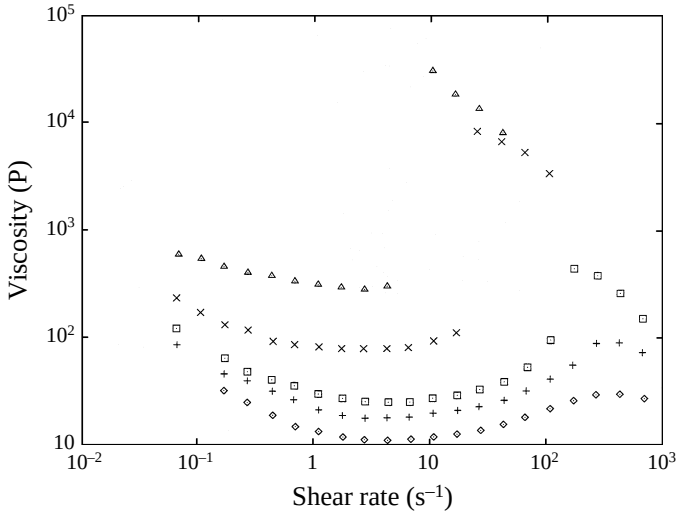

FIGURE 1. Viscosity versus shear rate from Hoffman (1972). $\diamond$, $\phi_v = 0.47$; $+$, $\phi_v = 0.49$; $\boxdot$, $\phi_v = 0.51$; $\times$, $\phi_v = 0.55$; $\triangle$, $\phi_v = 0.57$.

Chow & Zukoski 1995*a* and Laun *et al*. 1992), as well as in other types of suspensions. In this work, our interest is shear thickening in monodisperse suspensions of repulsive particles. Below, the current understanding of shear thickening in these systems is reviewed. We then describe the objective of the current study, which is to gain a better understanding of the origins of order–disorder transitions that are related to shear thickening in these types of suspensions.

In part because of its negative impact on industrial processes, shear thickening in repulsive systems has been extensively studied over the last few decades. As a result, there is a considerable body of knowledge regarding the rheological and microstructural changes associated with this phenomenon. An example is the work of Hoffman (1972), who measured shear-induced rheological and microstructural changes in monodisperse suspensions of sterically stabilized spheres. Measured viscosities from this study are shown in figure 1 and indicate that shear thickening can be severe at high densities. In particular, at a volume fraction $\phi_v = 0.57$, Hoffman (1972) measured a discontinuous jump in which the viscosity increased about 100-fold. Although shear thickening had been observed prior to this study (see e.g. Metzner & Whitlock 1958), Hoffman's measurements were the first evidence of discontinuous shear thickening.

Microstructural changes associated with the viscosity variation in figure 1 were inferred from light diffraction patterns, obtained by passing a collimated beam of white light through the sheared suspension. From these patterns, Hoffman (1972) (see also Hoffman 1991) determined that the shear thickening in this system was associated with an order–disorder transition of the suspension microstructure. Below the critical shear rate at which this transition occurred, the microstructure consisted of hexagonally close-packed layers of particles oriented parallel to planes of constant velocity. Above the critical shear rate, Hoffman's diffraction patterns indicated a completely disordered or amorphous microstructure. Hoffman further conjectured that the viscosity increase associated with the order–disorder transition was due to particle collisions in the disordered state, and the absence of these collisions when the suspension was ordered.

Hoffman's results were criticized by Strivens (1976) and Chaffey & Wagstaff (1977), who believed that shear thickening was a machine artifact that could be avoided by reducing rheometer acceleration. However, since these earlier works, numerous other

studies of shear thickening in repulsive suspensions have been undertaken. These include Hoffman (1974), Willey & Macosko (1978), Boersma, Laven & Stein (1990), Boersma *et al*. (1991), Laun, Bung & Schmidt (1991), Laun *et al* (1992), Chen *et al*. (1994), and Chow & Zukoski (1995*a*, *b*), and they confirm many of Hoffman's findings. As a result, there now appears to be strong agreement that shear thickening in concentrated charge- and sterically stabilized, monodisperse suspensions occurs with an order–disorder transition of the suspension microstructure.

We note that the link between shear thickening and order–disorder transitions is not as obvious in polydisperse and hard-sphere suspensions. The recent work of Bender & Wagner (1996) for model hard-sphere suspensions suggests that shear thickening in these systems occurs in the absence of an order–disorder transition, with the viscosity increase due to the formation of clusters that do not exist at subcritical shear rates. A similar explanation has been advanced by D'Haene, Mewis & Fuller (1993).

With the link between microstructural transitions and shear thickening in repulsive monodisperse suspensions well established, a number of investigators have developed models to predict the onset of disorder, and hence the onset of shear thickening. Hoffman (1974) proposed that observed microstructural transitions might be due to an instability of the layered configurations, with the layered configurations unstable above the critical shear rate. In his view, ordered layers become unstable at the shear rate where hydrodynamic torques acting on the particle layers begin to exceed torques arising from repulsive interparticle forces. He believed that this imbalance would cause particles to be ejected from the layers, leading to a loss of microstructural order. Based on this idea, Hoffman (1974) developed a mathematical model to predict the critical shear rate for the onset of shear thickening. However, this model was never rigorously tested.

More recently, a model predicting the onset of shear thickening has been advanced by Boersma *et al*. (1990). Somewhat similar in concept to the model of Hoffman (1974), their treatment is based on the hypothesis that charge-stabilized suspensions begin to become disordered, and shear thicken, at the shear rate where hydrodynamic forces acting on the suspended particles begin to exceed forces due to electrostatic repulsion. In their model, they consider two spheres approaching along their line of centres and assume the critical shear rate occurs when the net force on each particle is zero. Using simplified expressions for these forces, and assuming particles are monosized and hexagonally close-packed within layers, Boersma *et al*. (1990) obtained an expression for the critical shear rate $\dot{\gamma}_c$ of the form

$$\dot{\gamma}_c = C\{(\phi_{v_m}/\phi_v)^{1/3} - 1\}. \tag{1}$$

In (1), C is a constant determined by the properties of the particles and the suspending liquid, ϕ_v is the volume fraction of suspended particles, and ϕ_{v_m} is the maximum volume fraction attainable for the assumed microstructure. Predictions obtained from this model have been compared to experimental data with varying degrees of agreement. Boersma *et al*. (1990) found reasonable agreement between model predictions and their experimentally measured critical shear rates. However, Chen *et al*. (1994) found the model severely overpredicted their measured values of $\dot{\gamma}_c$.

Despite reasonable agreement with their own experimental data, there appears to be a flaw in the model of Boersma *et al*. (1990). Since they assumed hydrodynamic forces to be due entirely to the effect of the thin lubrication layer between the particles, both hydrodynamic and electrostatic forces are repulsive as the particle separation approaches zero. Therefore, the net force on the particles in their model can never be zero.

Chow & Zukoski (1995*a*) have proposed a model of shear thickening in repulsive systems that is somewhat different from the models discussed above. They believe that commonly observed order–disorder transitions and shear thickening are two distinct phenomena, with disorder a necessary but not sufficient condition for shear thickening. In agreement with others, they believe the onset of disorder is due to an instability that arises from an imbalance of hydrodynamic and interparticle forces. However, they believe shear thickening will occur only if bulk deformation rates exceed particle diffusion rates. In their view, this leads to the formation of particle clusters, which if sufficiently large can span the rheometer gap and generate the large stresses characteristic of shear thickening. Data presented in Chow & Zukoski (1995*b*) are in agreement with this model and indicate that moderately dense repulsive suspensions will disorder without shear thickening. However, since particle diffusivities decrease with increasing volume fraction, the model of Chow & Zukoski (1995*a*) does suggest a correlation between shear thickening and order–disorder transitions in very dense suspensions. In agreement with Hoffman (1972), the data of Chow & Zukoski (1995*b*) do indicate such a correlation.

A common element of the models discussed above is the view that observed order–disorder transitions are due to an imbalance of forces or torques acting on the suspended particles. However, since particle inertia is extremely small in colloidal suspensions, particles should be force- and torque-free in the range of shear rates at which disordering is typically observed. This suggests that the mechanism responsible for these transitions cannot be a force or torque imbalance.

However, there does appear to be substantial evidence to suggest that observed order–disorder transitions in repulsive suspensions are due to a microstructural instability. For non-aqueous suspensions of polyvinyl chloride particles, Willey & Macosko (1978) measured viscosities at a number of discrete shear rates and observed discontinuous shear thickening at the highest shear rate in this range. Subsequent measurements at shear rates intermediate to the two highest discrete values indicated a temporally increasing viscosity. The observed rheopexy continued until the sample was ejected from the rheometer. Laun *et al.* (1991) and Chen *et al.* (1994) found that suspensions subjected to a step change in shear rate from subcritical to supercritical values would retain the low viscosity associated with the subcritical shear rate. However, after short periods of supercritical shearing, the viscosity would abruptly increase to a value more characteristic of the supercritical shear rate. Laun *et al.* (1991, 1992) have observed metastable low viscosities at shear rates in excess of $\dot{\gamma}_c$. In addition, in tests in which the imposed shear stress was ramped up to some maximum value and then ramped down to its original value, Laun *et al.* (1991) observed distinct hysteresis behaviour, with the critical shear rate marking the onset of shear thickening significantly larger during the upward ramp than during the downward ramp. The results of these investigations are consistent with the view that order–disorder transitions in charge- and sterically stabilized suspensions arise from an instability of the layered configurations. Furthermore, observations of metastability and hysteresis suggest the importance of both a linear and a finite-amplitude instability.

With recent advances in simulation methods and computer technology, dynamic simulation has become a viable tool for investigations of shear thickening. Stokesian Dynamics (Brady & Bossis 1988) has been employed for a number of these studies and has confirmed many experimental findings. Brady & Bossis (1985) employed Stokesian Dynamics to investigate the behaviour of moderate-density charge-stabilized suspensions. The results of their simulations indicated that the suspensions shear thicken, a result they attribute to the formation of particle clusters. Brady & Bossis

(1988) used an analogous technique to simulate suspensions in narrow gaps and observed the formation of gap-spanning clusters. Chow & Zukoski (1995*a*) believe such clusters are responsible for shear thickening in very dense charge- and sterically stabilized suspensions. More recently, Boersma, Laven & Stein (1995) used Stokesian dynamics to investigate the behaviour of suspensions in which particles experience both attractive and repulsive forces. In agreement with experimental data, their results indicate that shear thickening is associated with a microstructural transition from ordered layers to an amorphous state.

Despite numerous investigations of shear thickening in monodisperse, charge- and sterically stabilized suspensions, the basic mechanism responsible for the underlying order–disorder transition that triggers shear thickening is still unknown. The goal of the present investigation is to determine the nature of this mechanism. In particular, we suggest that the observed order–disorder transitions in dense repulsive systems are due to an instability of the layered configurations existing at subcritical shear rates. Confirmation of this hypothesis will require measurement of transient particle motions in the suspensions. For the colloidal suspensions of interest here, these motions are extremely small and cannot be readily measured experimentally. However, microstructural information is readily available from dynamic simulation. Therefore, for this investigation Stokesian Dynamics will be employed. Stokesian Dynamics has been used successfully in a number of other rheological studies (see e.g. Bonnecaze & Brady 1992; Chang & Powell 1993; Boersma *et al.* 1995; Dratler & Schowalter 1996), and was selected for this work because it provides both bulk rheological properties and detailed microstructural information.

The simulation method used for this work is described in §2. In §3 our major findings are presented. Observed rheological and microstructural transitions are discussed in §3.1 where they are compared to available experimental data. In §3.2, we discuss the transient evolution of the rheology and microstructure and present evidence supporting our view that this evolution is due to a linear instability. In §3.3, we present a linear stability analysis which describes, in qualitative terms, the microstructural changes observed in the simulations. The effect of system size on our simulations is discussed in §3.4. Concluding remarks are presented in §4.

2. Simulation method

For the simulations discussed here we match the parameters to experiments reported by Boersma *et al.* (1990). Their suspension was monodisperse and consisted of charge-stabilized polystyrene spheres dispersed at a volume fraction of $\phi_v = 0.57$ in a mixture of glycerin and water. Shear thickening was first detected at a shear rate of $\dot{\gamma} \sim 1\ \mathrm{s}^{-1}$. Other relevant properties of this suspension are listed in table 1.

Given the physical characteristics of the suspension (see table 1), it is easily determined that the dominant forces controlling particle motion are hydrodynamic and repulsive in nature. Therefore, Brownian motion will be neglected in our simulations. In addition, because the particle Reynolds number is approximately zero, Stokesian Dynamics is used to simulate the sheared suspension. Stokesian Dynamics has been outlined in great detail in a number of papers (see e.g. Bossis & Brady 1984; Brady & Bossis 1985, 1988; Durlofsky, Brady & Bossis 1987; Brady *et al.* 1988; Bonecaze & Brady 1992) and the reader is referred to these works for an extended discussion of the method. Here, we will describe only those features essential for an understanding of the present work.

To facilitate simulation of the experiments described above, which were conducted

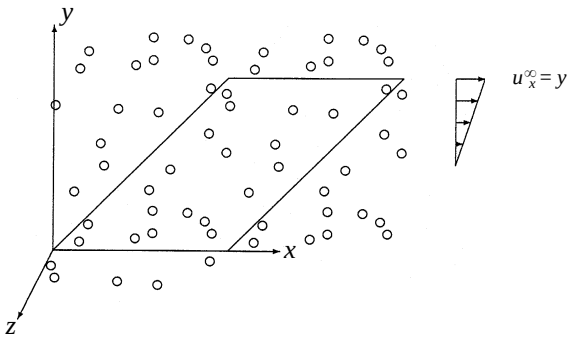

FIGURE 2. Schematic representation of computational domain. Domain contains N particles that all lie in the (x, y)-plane. Prior to shear the domain is square with dimensions $h_{cell} \times h_{cell}$. Suspension is subjected to an imposed shear flow given by $\boldsymbol{u}^\infty = (y, 0, 0)$.

Volume fraction, ϕ_v	0.57
Particle radius, a	0.805 μm
Solvent viscosity, η_s	0.140 Pa s
Debye decay length, $1/\kappa$	16.9 nm
Surface potential, ψ_0	31 mV
Solvent dielectric constant, ϵ	48.65

TABLE 1. Parameters from experiments of Boersma *et al.* (1990).

using a concentric-cylinder rheometer, the suspension is assumed infinite in extent and subject to an imposed velocity field given by

$$\boldsymbol{u}^\infty = (y, 0, 0), \tag{2}$$

where the vector $\boldsymbol{u}^\infty$ denotes the bulk translational velocity of the suspension and y denotes distance in the shear gradient direction. In (2) and for the remainder of this paper, displacements are non-dimensionalized by the sphere radius a, time by the reciprocal of the imposed shear rate $1/\dot{\gamma}$, translational velocities by $\dot{\gamma}a$, rotational velocities by $\dot{\gamma}$, viscosity by the solvent viscosity η_s, strain rates by $\dot{\gamma}$, forces by $6\pi\eta_s a^2\dot{\gamma}$, and torques and stresslets by $6\pi\eta_s a^3\dot{\gamma}$. With this scaling, dimensionless time is equal to shear strain. To reduce computational costs of the simulations, particles are restricted to a monolayer coincident with the (x, y)-plane, the plane of shear. The monolayer particle concentration equivalent to the volume fraction of Boersma *et al.*'s experiment is obtained from the expression $\phi_a = 3\sqrt{3}\phi_v/4$ (Brady & Bossis 1985), where ϕ_a is the areal fraction of particles in the monolayer. For $\phi_v = 0.57$, this expression gives $\phi_a = 0.74$. The scale factor $3\sqrt{3}/4$ is the ratio of areal to volume fraction at maximum packing, with maximum packing associated with a square lattice in two dimensions and hexagonally close-packed layers in three dimensions. The suspension geometry and the coordinate system are shown in figure 2.

To model a monolayer suspension of infinite extent, we consider a finite system of N particles that is periodically replicated through the (x, y)-plane. Prior to shearing, this N-particle system resides in a square computational domain of dimensions $h_{cell} \times h_{cell}$. The dynamics of this system are governed by a force balance on the suspended particles of the form

$$\boldsymbol{F}_h + \boldsymbol{F}_p = \boldsymbol{0}, \tag{3}$$

where inertia has been neglected due to the small size of the suspended particles. In (3) the vector $\boldsymbol{F}_h$ contains the hydrodynamic forces and torques exerted on the N suspended particles by the fluid and the vector $\boldsymbol{F}_p$ contains the forces and torques exerted on each of the suspended particles by interparticle forces. For the monolayer suspensions of interest in this work, forces associated with each particle are restricted to the (x, y)-plane while torques associated with each particle are restricted to the z-direction. As a result, the vectors in (3) have dimension $3N$.

Durlofsky *et al.* (1987) have shown that the hydrodynamic force and torque vector $\boldsymbol{F}_h$ can be modelled using

$$\boldsymbol{F}_h = -\boldsymbol{R}_{FU} \cdot (\boldsymbol{U} - \boldsymbol{U}^\infty) + \boldsymbol{R}_{FE} : \boldsymbol{E}^\infty. \tag{4}$$

In (4), $\boldsymbol{U}$ contains the translational and rotational velocities of the N suspended particles; $\boldsymbol{U}^\infty$ contains the translational and rotational components of the bulk velocity that would exist at the particle centres in the absence of the particles; and $\boldsymbol{E}^\infty$ contains the e_{xx}, e_{yy}, and e_{xy} components of the bulk rate-of-strain tensor that would exist at the particle centres in the absence of the particles. For the bulk velocity field given by (2), the rate-of-strain tensor is constant with components $e_{xx} = e_{yy} = 0$ and $e_{xy} = 1/2$. Because of the monolayer geometry and the assumed form of the bulk flow, translational velocities associated with the particles and the bulk motion are restricted to the (x, y)-plane while rotational velocities associated with the particles and the bulk motion are restricted to the z-direction. Therefore, all vectors in (4) have dimension $3N$.

The quantities $\boldsymbol{R}_{FU}$ and $\boldsymbol{R}_{FE}$ in (4) are configuration-dependent resistance tensors and are derived from an integral solution of Stokes equations. These tensors include far-field hydrodynamic interactions, including interactions involving particles that reside in image domains, and near-field lubrication effects. The far-field interactions are efficiently incorporated into (4) using an Ewald sum (see Brady *et al.* 1988). Using the Ewald sum, the strength of the far-field hydrodynamic interactions decays rapidly with increasing distance between the computational domain and image domains. Therefore, only image domains relatively close to the computational domain need be explicitly included in the formulation of (4). In this work, image domains are included if they abut the computational domain, or if they abut image domains that abut the computational domain. In addition, to maintain positive definiteness, the monolayer must also be periodically replicated in the z-direction. These periodic images are located at $z = \pm z_{cell}$ and $z = \pm 2z_{cell}$, with $z_{cell} = 100h_{cell}$. The computational domain is located at $z = 0$. In tests we have found that variations in z_{cell} and variations in the number of image domains employed in the formulation of (4) do not significantly influence simulation results.

Combining (3) and (4) leads to

$$\boldsymbol{R}_{FU} \cdot (\boldsymbol{U} - \boldsymbol{U}^\infty) = \boldsymbol{F}_p + \boldsymbol{R}_{FE} : \boldsymbol{E}^\infty, \tag{5}$$

which is a system of linear algebraic equations of dimension $3N$. For a known configuration of particles, and a known dependence of $\boldsymbol{F}_p$ on particle configuration, equation (5) can be solved for the unknown velocities $\boldsymbol{U}$. Therefore, given a known initial configuration of particles, the temporal variation of particle positions and velocities can be obtained through solution of (5) and numerical integration of $\boldsymbol{U}$. For this work, a fourth-order Adams–Bashforth scheme (Conte & de Boor 1980) is used for the numerical integration. To reduce the computational costs associated with computing $\boldsymbol{R}_{FU}$ and $\boldsymbol{R}_{FE}$, the far-field contributions to these tensors, which vary slowly with time, are recomputed at time intervals of T_{inv} instead of at every time step.

In this work, repulsive interparticle forces are assumed well-described by the

constant-potential Derjaguin formula (Russel, Saville & Schowalter 1989), and are computed using

$$\boldsymbol{F}_{p}^{\alpha\beta} = \left(\frac{\tau}{\dot{\gamma}^*}\frac{\mathrm{e}^{-\tau h}}{1+\mathrm{e}^{-\tau h}} + \frac{\tau_1}{\dot{\gamma}_1^*}\frac{\mathrm{e}^{-\tau_1 h}}{1+\mathrm{e}^{-\tau_1 h}}\right)\frac{\boldsymbol{r}_{sep}}{|\boldsymbol{r}_{sep}|}. \tag{6}$$

The first term in (6) represents forces arising from the charge stabilization of the particles, while the second term is an additional repulsive force that is employed to prevent particle overlaps. For the high particle concentrations of interest in this work, Dratler & Schowalter (1996) have shown that overlaps can be quite numerous in disordered suspensions and can significantly impact the microstructure and rheology. Therefore, following this earlier work, particle overlaps are prevented by employing the short-range repulsive force included in (6). This force is also represented by the constant-potential Derjaguin formula, although its precise form is unimportant provided it rapidly decays to zero with increasing particle separation.

In (6), $\boldsymbol{F}_{p}^{\alpha\beta}$ is the force on particle α due to particle β, $\boldsymbol{r}_{sep}$ is the centre-to-centre separation vector directed from particle β to particle α, $1/\tau$ (with $\tau = a\kappa$ and κ defined in table 1) is a dimensionless double-layer thickness, and $h = |\boldsymbol{r}_{sep}| - 2$. The parameter $\dot{\gamma}^*$ is a dimensionless shear rate equal to $(6\pi\eta_s a^2\dot{\gamma})/(2\pi\epsilon\epsilon_0\psi_0^2)$ where ϵ is the dielectric constant of the suspending fluid, ϵ_0 is the permittivity of free space, and ψ_0 is the surface potential of the particles. For the parameters listed in table 1, $\tau = 47.656$ and $\dot{\gamma}^* = 0.6575\dot{\gamma}$. The parameters controlling the second term in (6) are taken to be $\tau_1 = 10^6$ and $\dot{\gamma}_1^* = 1$. Dratler & Schowalter (1996) have shown these values to be adequate for preventing overlaps when simulating sheared suspensions of non-Brownian hard spheres, and that computed results are not significantly affected by variations in these parameters for areal fractions at least as high as 0.60. Finally, in the absence of information to the contrary, we will assume spherically symmetric charge distributions on the suspended particles. Therefore, torques due to electrostatic effects are identically zero.

We note that the second term in (6) does not prevent disorder or the formation of particle clusters. It simply prevents the occurrence of unphysical particle overlaps. This has been shown by Dratler & Schowalter (1996), who simulated sheared suspensions of non-Brownian hard spheres. Their results indicated the formation of particle clusters irrespective of whether this additional repulsion was employed. Furthermore, results discussed in §3.1 show that particle clusters form when the suspension shear thickens. This is consistent with experimental and computational evidence of others (see e.g. Bossis & Brady 1989; D'Haene *et al.* 1993; Phung, Brady & Bossis 1996; Bender & Wagner 1996).

The suspension viscosity η is defined as the volume-average shear stress divided by the shear rate $\dot{\gamma}$, and can be written

$$\eta = 1 + 3\phi_a\frac{1}{N}\sum_{\alpha=1}^{N} S_{h_{xy}}^{\alpha} + 3\phi_a\frac{1}{N}\sum_{\alpha=1}^{N}\sum_{\beta=1}^{\alpha-1} F_{p_x}^{\alpha\beta}(y_\beta - y_\alpha) \tag{7}$$

(see Bonnecaze & Brady 1992). In (7), $F_{p_x}^{\alpha\beta}$ is the x-component of interparticle force exerted on particle α by particle β, $y_\beta - y_\alpha$ is the distance in the shear-gradient direction from the centre of particle α to the centre of particle β, and $S_{h_{xy}}^{\alpha}$ is the x,y-component of the hydrodynamic stresslet exerted on particle α by the fluid. The stresslet $S_{h_{xy}}^{\alpha}$ is obtained from the expression

$$\boldsymbol{S}_h = -\boldsymbol{R}_{SU}\cdot(\boldsymbol{U} - \boldsymbol{U}^{\infty}) + \boldsymbol{R}_{SE};\boldsymbol{E}^{\infty}, \tag{8}$$

where $\boldsymbol{S}_h$ contains the three non-zero independent components of the hydrodynamic stresslet, $S_{h_{xx}}$, $S_{h_{yy}}$, and $S_{h_{xy}}$, exerted on each of the N particles; and the resistance ten-

sors $\boldsymbol{R}_{SU}$ and $\boldsymbol{R}_{SE}$ are derived in a manner analogous to $\boldsymbol{R}_{FU}$ and $\boldsymbol{R}_{FE}$. For each simulation, the time average of η, denoted by $\bar{\eta}$, is computed in the temporal interval $T_e \leqslant t \leqslant T_s$ where T_s is the final time of the simulation and T_e is the equilibration time of η. The equilibration time is conservatively taken to be the time at which the running average of η ceases to vary significantly. Statistical errors in $\bar{\eta}$ are determined using the sub-average method outlined in Allen & Tildesley (1987).

3. Results and discussion

In this section, we present results of Stokesian Dynamics simulations of the suspension described in §2. In §3.1, we discuss rheological and microstructural transitions that occur when the shear rate of the imposed flow is varied from 0.1 s^{-1} to 200 s^{-1}. Viscosities obtained from these simulations are compared to analogous experimental measurements of Boersma *et al.* (1990). In §3.2, we discuss temporal aspects of observed shear thickening, and associated order–disorder transitions, and the effect of shear rate on these transitions. In §3.3, we present results of a stability analysis which supports our contention that the onset of disorder is due to an instability of the sliding layer microstructure. Finally, in §3.4 we discuss the effect of system size on our results.

Simulations were performed using 25, 36, 81 and 100 particles. Results for $N = 25$ are presented in §§3.1 and 3.2. Results of simulations employing 36, 81 and 100 particles are presented in §3.4, where they are compared to our 25-particle results. Simulations of ordered suspensions were performed using a time step of $\Delta t = 10^{-3}$. However, because of the need to employ a short-range repulsive force to prevent particle overlaps (see §2), a much smaller time step, $\Delta t = 7.8125 \times 10^{-6}$, was required for simulations of disordered suspensions. For all simulations, $T_{inv} = 0.1$. To ensure that our results would not change significantly with variations in Δt or T_{inv}, simulations of ordered suspensions were repeated with $\Delta t = 5 \times 10^{-4}$ and $T_{inv} = 0.1$, and with $\Delta t = 10^{-3}$ and $T_{inv} = 0.05$. With these changes in Δt and T_{inv}, computed values of $\bar{\eta}$ varied by less than 1%. Because of the higher computational cost of simulating disordered suspensions, the effect of Δt on computed results was inferred from simulations for which $\dot{\gamma}^* = \infty$. For this value of $\dot{\gamma}^*$, the charge-stabilized suspension described in §2 is equivalent to a suspension of non-Brownian hard spheres. Simulations with $\dot{\gamma}^* = \infty$ were performed with $\Delta t = 7.8125 \times 10^{-6}$ and 3.90625×10^{-6}, with $T_{inv} = 0.1$ for both runs. For these simulations, $\bar{\eta}$ differed by less than 10%. In addition, since far-field hydrodynamic interactions are expected to be of secondary importance in concentrated disordered suspensions, the effect of varying T_{inv} was not quantified. Simulations were typically run for 500 dimensionless time units ($T_s = 500$) when the suspension remained ordered, and for about 100–150 time units when the suspension was disordered. With the exception of N, the effect of which is discussed in §3.4, variations in other numerical parameters were found to have little influence on computed results.

3.1. *Rheology and microstructure*

The rheological behaviour of the suspension of interest, when subjected to an imposed linear shear flow, was determined by performing simulations for a number of shear rates in the range $0.1 \leqslant \dot{\gamma} \leqslant 200\ s^{-1}$. Simulations were performed sequentially, beginning with the lowest shear rate ($\dot{\gamma} = 0.1\ s^{-1}$) and finishing with the highest shear rate ($\dot{\gamma} = 200\ s^{-1}$). For $\dot{\gamma} = 0.1\ s^{-1}$, the initial configuration consisted of particles randomly positioned in the computational domain. For $\dot{\gamma} > 0.1\ s^{-1}$, initial conditions were taken to be particle positions associated with $t = T_s$ from the preceding

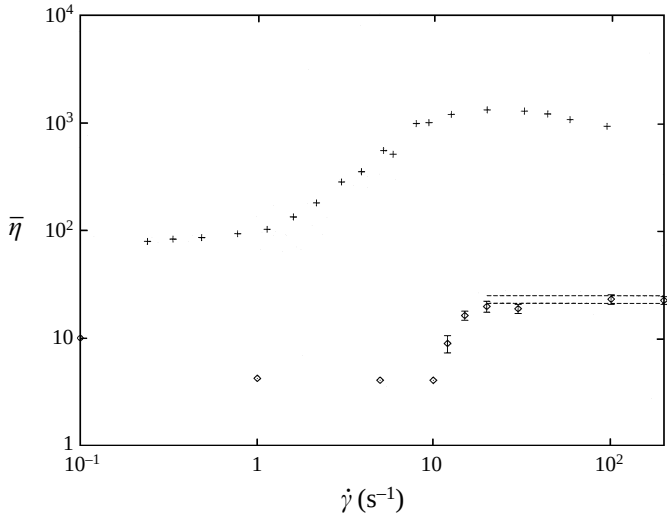

FIGURE 3. Relative viscosity $\overline{\eta}$ as a function of shear rate $\dot{\gamma}$ from Stokesian Dynamics simulation of a monolayer suspension of charge-stabilized rigid spheres in a bulk linear shear flow, Φ. For comparison, experimental data of Boersma *et al.* (1990) (+) are also shown. For the simulations: $\phi_a = 0.74$, $\tau = 47.656$, $N = 25$, and error bars are omitted when smaller than the symbol. For $\dot{\gamma} \geqslant 12\ s^{-1}$, additional repulsion with $\tau_1 = 10^6$ and $\dot{\gamma}_1^* = 1$ was used to prevent overlapping particles. Viscosity in the limit $\dot{\gamma} \to \infty$ (-----) is also shown, with the two lines representing the upper and lower bounds of the 95% confidence interval associated with $\overline{\eta}(\dot{\gamma} = \infty)$. For the experimental data: $\phi_v = 0.57$ and the suspension consists of polystyrene spheres of diameter 1.61 μm dispersed in a mixture of glycerin and water.

simulation. For $\dot{\gamma} > 10\ s^{-1}$, the suspension exhibited varying degrees of disorder. Therefore, as described in §2, particles were subjected to an additional repulsive force in order to prevent particle overlaps. For this additional repulsion, $\tau_1 = 10^6$ and $\dot{\gamma}_1^* = 1$.

For these simulations, the time-averaged viscosity $\overline{\eta}$ is shown as a function of shear rate in figure 3. For $\dot{\gamma} < 1\ s^{-1}$ the suspension is shear thinning, with $\overline{\eta}$ decreasing from near 10 to about 4 when $\dot{\gamma}$ is increased from 0.1 to $1\ s^{-1}$. For $\dot{\gamma} > 10\ s^{-1}$, shear thickening is observed, with $\overline{\eta}$ increasing about five-fold between shear rates of 10 and $20\ s^{-1}$. For $\dot{\gamma} \geqslant 20\ s^{-1}$, $\overline{\eta} \approx 20$. In the limit $\dot{\gamma} \to \infty$, the charge-stabilized suspension of interest here is equivalent to a suspension of non-Brownian hard spheres. The viscosity associated with such a suspension, computed using Stokesian Dynamics, is also shown in figure 3 (dashed lines) and is seen to agree quite well with our simulated viscosities in the range $20 \leqslant \dot{\gamma} \leqslant 200\ s^{-1}$. This suggests that when the suspension has completely shear thickened, it is rheologically indistinguishable from a suspension of non-Brownian hard spheres.

For comparison, experimentally measured viscosities obtained by Boersma *et al.* (1990) for the suspension described in table 1 are also shown in figure 3. The simulated viscosities and experimental data show the same qualitative features, including two viscosity plateaus separated by a region of shear thickening. However, computed and measured values of $\overline{\eta}$ differ by as much as two orders of magnitude. In addition, shear thickening occurs over a larger range of shear rate in the experiments than in the simulations. Although we do not have a definitive explanation of these differences, we believe we have ruled out two causes. First, we do not believe the observed differences are due to the number of particles used in our simulations. As will be discussed in detail in §3.4, we have performed simulations using 36, 81 and 100 particles and have

obtained viscosities similar to those shown in figure 3. Also, we do not believe the observed differences are due to our assumption of a two-dimensional microstructure. We have performed a small number of three-dimensional simulations and have obtained viscosities similar to the simulated viscosities shown in figure 3. However, because the number of three-dimensional simulations was limited, a definitive explanation of the observed differences will require further investigation. The observed discrepancies could be due in part to the absence of rheometer walls in our simulations, which precludes the formation of rheometer-gap-spanning clusters, or to some other physical aspect of the system that is missing from the numerical model. Gap-spanning clusters are believed by some (see e.g. Chow & Zukoski 1995*a*) to be the cause of shear thickening in charge- and sterically stabilized suspensions. However, for sheared suspensions of non-Brownian hard spheres, we have used our simulation code to obtain viscosities in good agreement with experimental data (see Dratler & Schowalter 1996). In addition, we have used our simulation code to replicate the simulations of charge-stabilized suspensions that were reported by Boersma *et al.* (1995). Their simulations are also of a monolayer suspension, but were performed at a much lower areal fraction ($\phi_a = 0.5454$). Therefore, their computed viscosities are not directly comparable to our results shown in figure 3 or to the experimental data of Boersma *et al.* (1990). However, when we performed simulations exactly as described by Boersma *et al.* (1995), our computed viscosities were very close to their computational results.

In agreement with established experimental data for dense monodisperse repulsive suspensions (see e.g. Hoffman 1972; Chen *et al.* 1994; Chow & Zukoski 1995*b*), the shear thickening observed in figure 3 is associated with an order–disorder transition of the suspension microstructure. This is illustrated in figure 4 where the pair distribution function $g(y)$ is shown for $\dot{\gamma} = 10$, 12, 15 s^{-1} and ∞. As noted above, the charge-stabilized suspension of interest here is equivalent to a suspension of non-Brownian hard spheres when $\dot{\gamma} = \infty$. The function $g(y)$ is the normalized probability that a particle resides at the cross-stream position $y_{ref}+y$ when another particle is known to reside at the cross-stream position y_{ref}. For $\dot{\gamma} = 10$ s^{-1} (figure 4*a*), $g(y)$ exhibits large peaks at $y \approx 2$ and $y \approx 4$. Between these peaks, $g(y) \equiv 0$. This indicates that the suspension is ordered in two-dimensional analogues of experimentally observed sliding layer configurations. These layers (actually strings since the suspension is two-dimensional) are perpendicular to the y-axis and are separated by slightly more than one particle diameter. In contrast, for $\dot{\gamma} = 15$ s^{-1} (figure 4*c*) the peaks in $g(y)$ are much smaller and broader than those observed for $\dot{\gamma} = 10$ s^{-1}. This change in $g(y)$ indicates a loss of long-range order, with particles no longer confined to distinct layers at this higher shear rate. For shear rates in excess of 15 s^{-1}, the suspension microsctructure, as characterized by $g(y)$, differs little from the microstructure at $\dot{\gamma} = 15$ s^{-1}. In addition, the similarity of $g(y)$ at $\dot{\gamma} = 15$ s^{-1} to $g(y)$ at $\dot{\gamma} = \infty$ (see figure 4*d*) suggests a supercritical microstructure that is characteristic of sheared suspensions of non-Brownian hard spheres. For $\dot{\gamma} = 12$ s^{-1}, the suspension microstructure alternates in time between periods of order and periods of disorder. The time interval between periods of order is non-uniform and ranges from about 15 to about 120 dimensionless time units. As a result, values of $g(y)$ at $\dot{\gamma} = 12$ s^{-1} (see figure 4*b*) are intermediate to those computed for $\dot{\gamma} = 10$ and 15 s^{-1}. Furthermore, since this temporal variation of microstructural order did not dissipate, even for simulations of nearly 1000 time units, we believe it is the correct long-time behaviour at this shear rate. In addition, similar transient variations in microstructural order have been observed experimentally by Chen *et al.* (1994) and Chow & Zukoski (1995*b*).

To illustrate more clearly the change in microstructure associated with shear

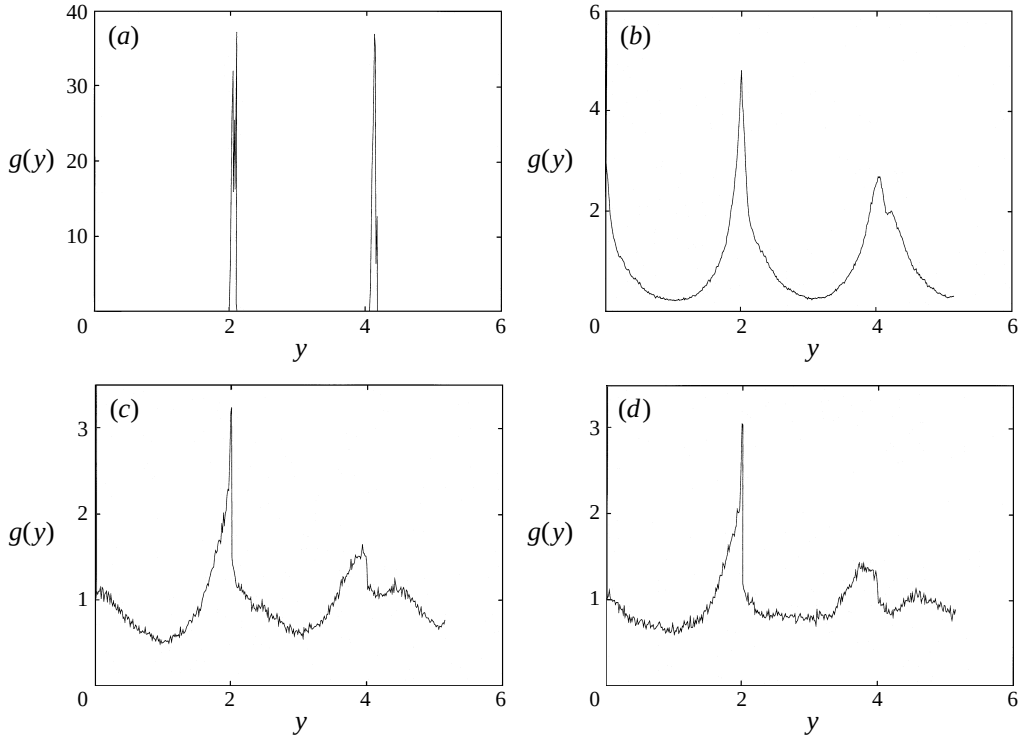

FIGURE 4. Pair distribution function $g(y)$ associated with some of the simulated viscosities shown in figure 3. $\phi_a = 0.74$, $\tau = 47.656$, $N = 25$. For $\dot{\gamma} = 12\ \mathrm{s}^{-1}$, $15\ \mathrm{s}^{-1}$ and ∞, additional repulsion with $\tau_1 = 10^6$ and $\dot{\gamma}_1^* = 1$ was used to prevent overlapping particles. (*a*) $\dot{\gamma} = 10\ \mathrm{s}^{-1}$, (*b*) $\dot{\gamma} = 12\ \mathrm{s}^{-1}$, (*c*) $\dot{\gamma} = 15\ \mathrm{s}^{-1}$ and (*d*) $\dot{\gamma} = \infty$.

thickening, instantaneous particle configurations for $\dot{\gamma} = 10$ and $15\ \mathrm{s}^{-1}$ are shown in figure 5. For $\dot{\gamma} = 10\ \mathrm{s}^{-1}$ (figure 5*a*), the suspension is highly ordered with particles confined to well-defined layers. In contrast, the configuration shown in figure 5(*b*), which is associated with a local maximum in η, is highly disordered and contains particle clusters aligned along the compressive axis of the bulk flow. The existence of these clusters would tend to support the view of Hoffman (1972) that shear thickening is due to particle collisions, or near collisions, in the disordered state. In addition, consistent with our earlier comments, the disordered particle configuration in figure 5(*b*) is similar to configurations observed in simulations of sheared suspensions of non-Brownian hard spheres (Dratler & Schowalter 1996). The appearance of these clusters in the shear-thickening region is also consistent with the findings of other investigators (see e.g. Bender & Wagner 1996; Phung *et al.* 1996, Bossis & Brady 1989). These investigations have suggested that the high viscosities in the shear-thickening region are due to the formation of large clusters similar to those seen in our simulations.

3.2. *Temporal evolution of microstructure*

To gain a better understanding of the order–disorder transition discussed in §3.1, it is useful to examine the temporal evolution of microstructure as the suspension moves from an ordered to a disordered state. Towards this end, we have conducted a number of simulations in which the suspension was initially ordered but was subjected to sustained supercritical shearing. The initial condition for these simulations was a configuration from a simulation for which $\dot{\gamma} = 10\ \mathrm{s}^{-1}$. At $\dot{\gamma} = 10\ \mathrm{s}^{-1}$, the suspension

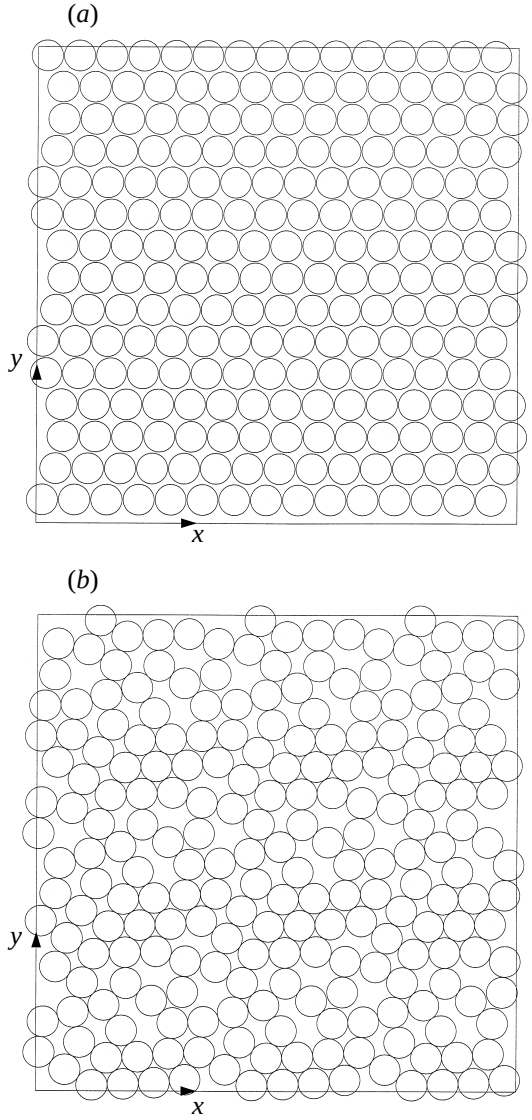

FIGURE 5. Instantaneous particle configurations for: (*a*) $\dot{\gamma} = 10\ \mathrm{s}^{-1}$, $t = 500$; (*b*) $\dot{\gamma} = 15\ \mathrm{s}^{-1}$, $t = 89.1$. The configuration in (*b*) is associated with the maximum instantaneous value of η attained at $\dot{\gamma} = 15\ \mathrm{s}^{-1}$. Configurations are from Stokesian Dynamics simulation of a monolayer suspension of charge-stabilized rigid spheres in a bulk linear shear flow. For $\dot{\gamma} = 15\ \mathrm{s}^{-1}$, additional repulsion with $\tau_1 = 10^6$ and $\dot{\gamma}_1^* = 1$ was employed to prevent particle overlaps. Flow is from left to right. For clarity, the computational domain has been replicated 9 times. $\phi_a = 0.74$, $\tau = 47.656$, $N = 25$.

microstructure consists of ordered layers. With this initial configuration, simulations were run for supercritical shear rates of $\dot{\gamma} = 12$, 15, 20 and 100 s^{-1}, with the simulations run sufficiently long in time so that the onset of disorder could be observed. In all cases, the additional repulsion described in §2 was used to prevent overlaps when the suspension was disordered. All other parameters were identical to those used for the simulations described in §3.1.

For the simulations described above, the time dependence of η is shown in figure 6. The viscosity is a useful quantity for assessing the level of disorder in the suspension

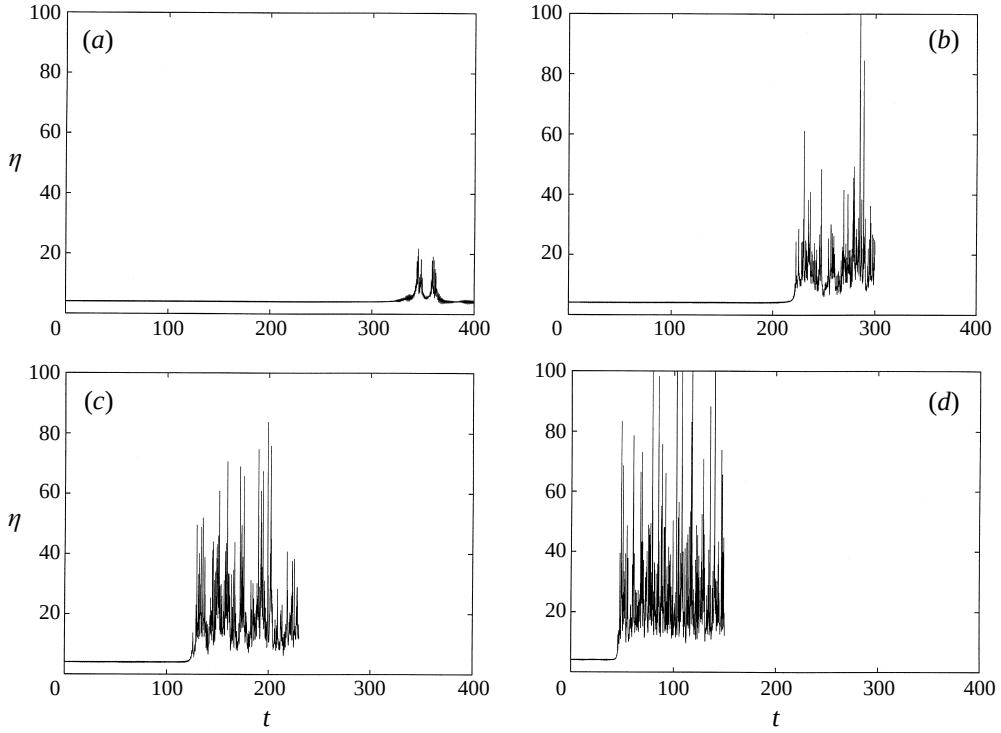

FIGURE 6. Temporal dependence of instantaneous viscosity η for several values of $\dot{\gamma}$, obtained from Stokesian Dynamics simulation of a monolayer suspension of charge-stabilized rigid spheres in a bulk linear shear flow. For all shear rates, the initial condition was an ordered particle configuration obtained from a simulation for which $\dot{\gamma} = 10\ \mathrm{s}^{-1}$. Additional repulsion with $\tau_1 = 10^6$ and $\dot{\gamma}_1^* = 1$ was employed to prevent overlapping particles. $\phi_a = 0.74$, $\tau = 47.656$, $N = 25$. (*a*) $\dot{\gamma} = 12\ \mathrm{s}^{-1}$, (*b*) $\dot{\gamma} = 15\ \mathrm{s}^{-1}$, (*c*) $\dot{\gamma} = 20\ \mathrm{s}^{-1}$ and (*d*) $\dot{\gamma} = 100\ \mathrm{s}^{-1}$.

since, for the high density considered, it changes significantly when the microstructure undergoes an order–disorder transition. For the areal fraction of interest, $\phi_a = 0.74$, η oscillates about a mean value of approximately 4 when the microstructure consists of layers. However, when the suspension is disordered η can attain values in excess of 100. For all shear rates shown, η is near 4 at small times, indicating the suspension remains ordered even when subjected to supercritical shearing. However, after a period of time the viscosity goes through a transition to much larger values, indicating a loss of microstructural order. The time required for the onset of this disorder is a decreasing function of shear rate, and ranged from approximately 330 dimensionless time units at $\dot{\gamma} = 12\ \mathrm{s}^{-1}$ to approximately 50 dimensionless time units at $\dot{\gamma} = 100\ \mathrm{s}^{-1}$. Recalling that time has been made dimensionless with the imposed shear rate, we note that the dimensional time required for the onset of disorder is about 55 times larger for $\dot{\gamma} = 12\ \mathrm{s}^{-1}$ than for $\dot{\gamma} = 100\ \mathrm{s}^{-1}$. For $\dot{\gamma} = 12\ \mathrm{s}^{-1}$ (figure 6*a*), the increase in viscosity at $t \approx 330$ is followed by a reduction in viscosity at $t \approx 360$, with η returning to a value near 4. This behaviour is indicative of an oscillation in time between periods of microstructural order and disorder, as first noted in §3.1.

To determine if ordered layers are indeed the preferred microstructure at $\dot{\gamma} = 10\ \mathrm{s}^{-1}$, simulations at this shear rate were initiated with both ordered and disordered configurations. When started from an ordered configuration, obtained from a simulation conducted at $\dot{\gamma} = 5\ \mathrm{s}^{-1}$, the suspension remained ordered for simulations of

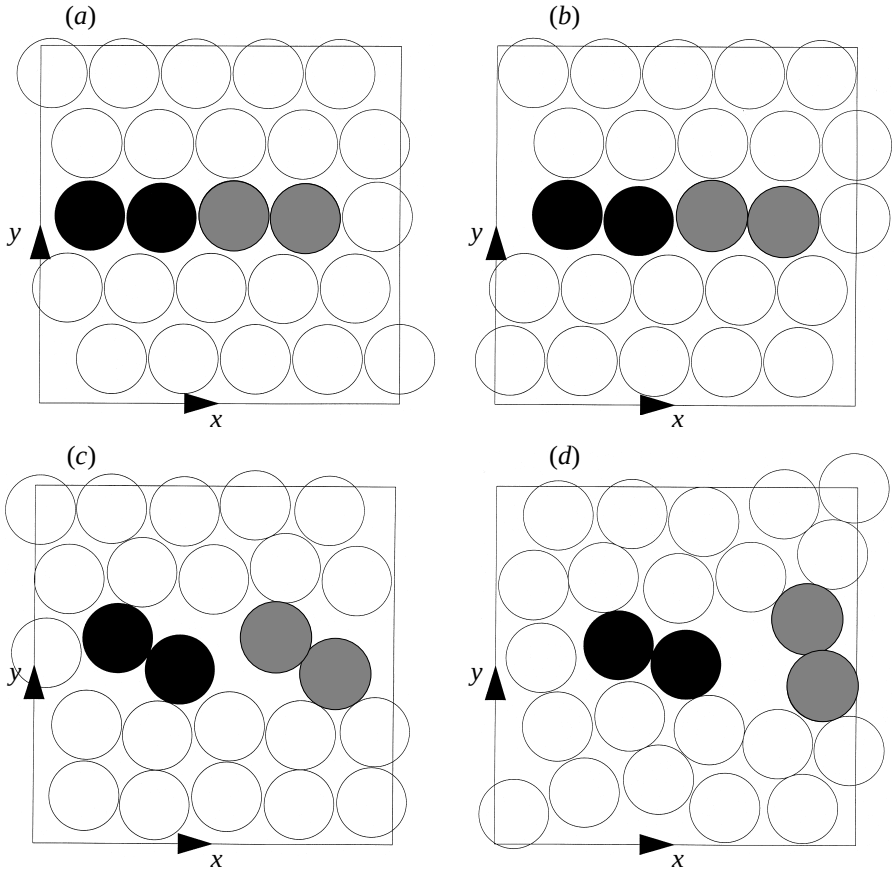

FIGURE 7. Instantaneous particle configurations at various times for the $\dot{\gamma} = 12\ \mathrm{s}^{-1}$ simulation whose viscosity is shown in figure 6(*a*), obtained from Stokesian Dynamics simulation of a monolayer suspension of charge-stabilized rigid spheres in a bulk linear shear flow. For this simulation, the initial condition was an ordered particle configuration obtained from a simulation for which $\dot{\gamma} = 10\ \mathrm{s}^{-1}$. Additional repulsion with $\tau_1 = 10^6$ and $\dot{\gamma}_1^* = 1$ was employed to prevent overlapping particles. Flow is from left to right. Particle doublets are identified by shading. $\phi_a = 0.74$, $\tau = 47.656$, $N = 25$. (*a*) $t = 300.0$, (*b*) $t = 315.0$, (*c*) $t = 342.0$ and (*d*) $t = 344.6$.

up to 6000 dimensionless time units. For simulations initiated with a disordered configuration, generated by randomly positioning particles in the computational domain, the suspension became ordered and remained ordered for simulations of up to 1500 dimensionless time units. The results suggest sliding layers are indeed the preferred asymptotic microstructure at $\dot{\gamma} = 10\ \mathrm{s}^{-1}$.

The persistence of low viscosities at supercritical shear rates, which is illustrated in figure 6, is consistent with the experimental measurements of Laun *et al.* (1991) and Chen *et al.* (1994). These investigators found that suspensions subjected to a step change in shear rate from subcritical to supercritical values would retain the subcritical value of the viscosity at the higher shear rate. However, after a period of supercritical shearing, their measurements indicated an increase in viscosity to a value characteristic of the higher shear rate.

To illustrate more clearly the onset of microstructural disorder, instantaneous particle configurations from the $\dot{\gamma} = 12\ \mathrm{s}^{-1}$ simulation discussed above are shown in figure 7 for $t = 300$, 315, 342 and 344.6. At $t = 300$ (figure 7*a*), particles are still largely

confined to layers. However, by $t = 315$ particles in the middle row have begun to aggregate with neighbouring particles to form doublets. Here we define a doublet as a pair of particles in which the upstream particle in the pair is offset in the positive y-direction from the downstream particle, and whose centre-to-centre separation vector exhibits clockwise rotation on average. This definition is somewhat arbitrary, but is useful for our purposes since it distinguishes particle pairs that rotate out of the layer, and disrupt the microstructure, from those that merely oscillate about their mean alignment. As the suspension is sheared, i.e. as time advances, the doublets rotate and begin to extend out of the layer. In addition, particle separation within the doublets decreases with time. By $t = 344.6$ (figure 7*d*), the doublets have rotated sufficiently to disrupt neighbouring layers and cause the suspension to disorder. These results strongly suggest that the onset of microstructural disorder in this type of suspension is due to the formation of doublets within particle layers, with these doublets rotating due to the imposed shear and disrupting the long-range order in the suspension. This mechanism was first proposed by Hoffman (1974). However, Hoffman (1974) believed the doublet rotation was due to an imbalance of hydrodynamically induced and repulsion-induced torques on the doublets. For the simulations, a torque imbalance cannot be responsible for the observed rotation because (3) imposes a force and torque balance on the suspended particles. Since the particles are force- and torque-free, the doublets must be torque-free. For similar reasons, the force imbalance hypothesis of Boersma *et al.* (1990) cannot explain the observed behaviour. As an additional clarification, we note that the observed doublets in figure 7 rotate much more slowly than individual particles in the suspension, with the grey-shaded doublet rotating by about 90° in about 50 time units. This is significantly slower than the rotation rate of individual particles.

Although figure 7 clearly shows the temporal evolution of particle doublets in the suspension, it is desirable to have a more quantitative measure of this evolution. A useful quantity in this regard is Δy_D, the distance in the shear-gradient direction between the centres of the two particles forming a doublet. This quantity has a value of zero when a doublet is perfectly aligned with the bulk velocity vector, and a value of approximately 2 when a doublet is perpendicular to the bulk velocity vector. For the simulations used to generate the viscosity data shown in figure 6, the temporal evolution of Δy_D associated with doublets in the suspension is shown in figure 8. This quantity is not a time- or configuration-average, but is associated with a single doublet in the suspension. In addition, Δy_D for $\dot{\gamma} = 30\ \mathrm{s}^{-1}$, obtained from a simulation performed exactly as described at the beginning of §3.2, is also shown. For all shear rates shown, Δy_D grows exponentially at small times with a growth rate that is an increasing function of the shear rate. For $\dot{\gamma} = 20$, 30 and $100\ \mathrm{s}^{-1}$, exponential growth ceases when Δy_D attains an $O(1)$ value, which it does when the suspension begins to exhibit a significant amount of disorder. In contrast, for $\dot{\gamma} = 15$ and $12\ \mathrm{s}^{-1}$ exponential growth ceases before Δy_D attains $O(1)$ values. These deviations from exponential growth are due to interactions with other doublets in the suspension. Despite these deviations, the results do suggest that the evolution of observed particle doublets is due to a linear instability of the sliding layer microstructure.

To check the temporal accuracy of these results, the $\dot{\gamma} = 30$ and $100\ \mathrm{s}^{-1}$ simulations used to generate Δy_D shown in figure 8 were repeated with $\Delta t = 10^{-3}$. These additional simulations were run for 75 and 40 time units, respectively. Because the minimum particle separation always exceeds 0.01 in these time intervals, the additional repulsion described by the second term in equation (6) is negligible and was not employed. In the original simulations a time step of $\Delta t = 7.8125 \times 10^{-6}$ was employed. For both $\dot{\gamma} = 30$

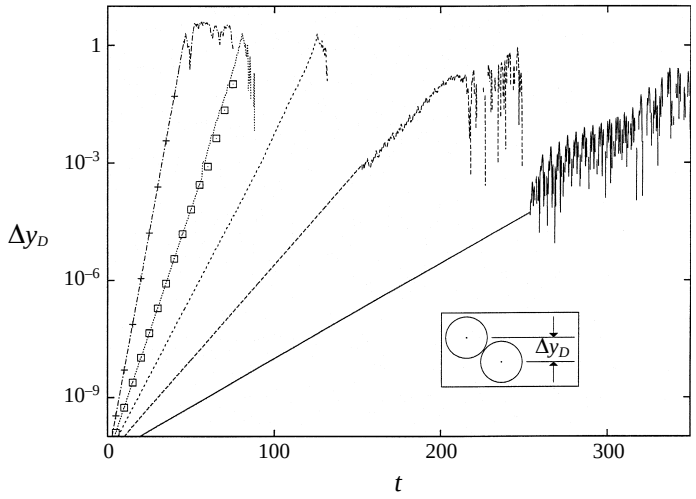

FIGURE 8. Temporal dependence of cross-stream separation distance Δy_D between particle centres in pairs that have formed doublets, obtained from Stokesian Dynamics simulation of a monolayer suspension of charge-stabilized rigid spheres in a bulk linear shear flow. For all shear rates, the initial condition was an ordered particle configuration obtained from a simulation for which $\dot{\gamma} = 10\ \mathrm{s}^{-1}$. Additional repulsion with $\tau_1 = 10^6$ and $\dot{\gamma}_1^* = 1$ was used to prevent overlapping particles. $\phi_a = 0.74$, $\tau = 47.656$, $N = 25$, $\Delta t = 7.8125 \times 10^{-6}$. ——, $\dot{\gamma} = 12\ \mathrm{s}^{-1}$; – – – –, $\dot{\gamma} = 15\ \mathrm{s}^{-1}$; - - - -, $\dot{\gamma} = 20\ \mathrm{s}^{-1}$; …, $\dot{\gamma} = 30\ \mathrm{s}^{-1}$; -·-·-, $\dot{\gamma} = 100\ \mathrm{s}^{-1}$. Symbols correspond to simulations performed without additional repulsion and with $\Delta t = 10^{-3}$, but identical in all other respects. ⊡, $\dot{\gamma} = 30\ \mathrm{s}^{-1}$; +, $\dot{\gamma} = 100\ \mathrm{s}^{-1}$.

and $100\ \mathrm{s}^{-1}$, the Δy_D from the $\Delta t = 10^{-3}$ simulations are shown in figure 8 and are seen to be in excellent agreement with the Δy_D obtained from the $\Delta t = 7.8125 \times 10^{-6}$ simulations. This indicates that the simulations used to compute the Δy_D shown in figure 8 are temporally well-resolved, and that the growth of Δy_D is not a numerical artifact.

Additional evidence supporting the view that observed order–disorder transitions are due to a linear instability of the sliding layer microstructure can be obtained from examination of transient motions associated with particles not directly involved in doublet formation. For the simulation where $\dot{\gamma} = 12\ \mathrm{s}^{-1}$, the temporal evolution of the cross-stream (y) component of a particle trajectory is shown in figure 9. For the data shown, variations due to the average motion of the configuration have been removed. The results, which pertain to the shaded particle shown in the inset of this figure, are oscillatory because of the shear-induced relative motion of adjacent particle layers. For $t \lesssim 275$, this oscillation has nearly constant amplitude and a dominant frequency equal to 1. However, for $t \gtrsim 275$, the amplitude of the oscillation begins to show visible growth. By $t \approx 350$, the amplitude of the oscillation is approximately 0.5, and the suspension has completely disordered.

For the data shown in figure 9, Fourier spectra were computed using a discrete Fourier transform for the time intervals defined by

$$220 + 10i \leqslant t < 270 + 10i, \quad \text{with} \quad i = 0, \ldots, 4. \tag{9}$$

Data were sampled at a rate of ten points per time unit, which gives a Nyquist frequency of five cycles per time unit. Since the trajectory data are not time periodic, a Hanning window (Bendat & Piersol 1986) was used to minimize side-lobe leakage.

In figure 10, amplitudes of computed Fourier coefficients are shown for the dimensionless frequency range $0 \leqslant f \leqslant 2$. The frequency $f = 1$ is associated with an

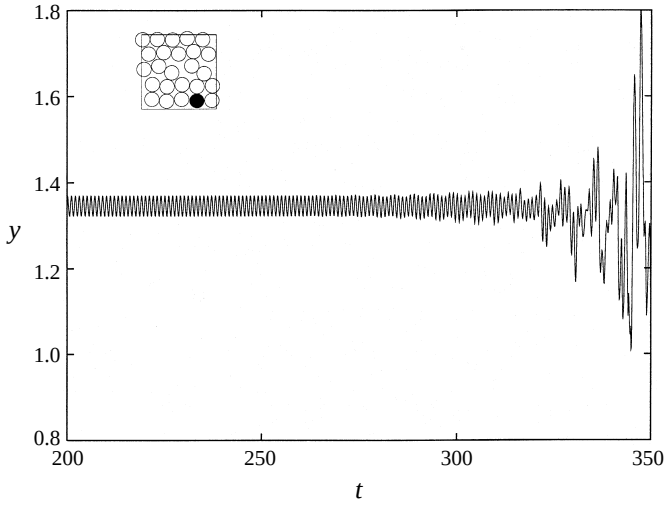

FIGURE 9. Temporal dependence of the cross-stream position y of the shaded particle shown in the inset, obtained from Stokesian Dynamics simulation of a monolayer suspension of charge-stabilized rigid spheres in a bulk linear shear flow. For this simulation, the initial condition was an ordered particle configuration obtained from a simulation for which $\dot{\gamma} = 10\ \mathrm{s}^{-1}$. Additional repulsion with $\tau_1 = 10^6$ and $\dot{\gamma}_1^* = 1$ was used to prevent overlapping particles. $\dot{\gamma} = 12\ \mathrm{s}^{-1}$, $\phi_a = 0.74$, $\tau = 47.656$, $N = 25$.

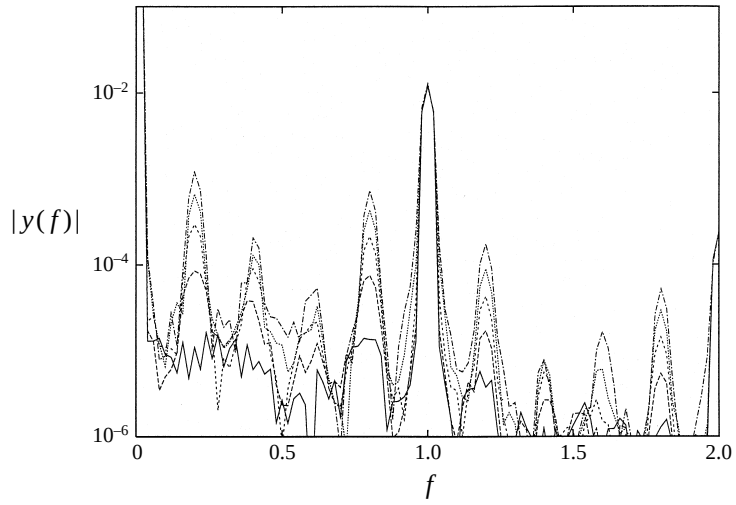

FIGURE 10. Amplitudes of Fourier coefficients obtained from decomposition of the trajectory data shown in figure 9. $\dot{\gamma} = 12\ \mathrm{s}^{-1}$, $\phi_a = 0.74$, $\tau = 47.656$, $N = 25$. ——, $220 \leqslant t < 270$; – – – –, $230 \leqslant t < 280$; ------, $240 \leqslant t < 290$; …, $250 \leqslant t < 300$, -·-·-, $260 \leqslant t < 310$.

oscillation of unit period, the dominant fluctuation for $t \lesssim 275$. Amplitudes associated with this frequency, and its first harmonic ($f = 2$), show little temporal growth. In contrast, for $0 < f < 1$ and $1 < f < 2$ amplitudes exhibit significant temporal growth, with pronounced maxima at frequencies of $f = 0.2$, 0.8, 1.2 and 1.8. The amplitudes associated with these maxima grow exponentially, to an approximate degree, providing additional evidence that the sliding layer configurations are linearly unstable above the critical shear rate. Fourier spectra were also computed in time intervals of differing width, with little effect on the results.

Finally, although sliding layers appear to be the preferred asymptotic microstructure at $\dot{\gamma} = 10\ \mathrm{s}^{-1}$, we did observe particle doublets at this shear rate. However, in contrast to observations at higher shear rates, these doublets appeared intermittently and had relatively small values of Δy_D. As a result, their appearance did not cause the suspension to disorder or shear thicken. The presence of these doublets in configurations used to initiate simulations at supercritical shear rates did result in a more rapid onset of disorder than occurred in simulations where doublets were not present in initial configurations. However, Δy_D associated with doublets in these supercritical simulations still grew exponentially, suggesting that this growth was still due to a linear instability of the sliding layer microstructure.

3.3. *Linear stability analysis*

To substantiate further our contention that the loss of microstructural order in monodisperse charge-stabilized suspensions is due to a linear instability, we have analysed the stability of the sliding layer microstructure. We propose that the ordered layers become unstable because of the effect of lubrication interactions between adjacent particles within each layer and the effect of the spatially varying velocity field. Therefore, we will consider the stability of a single layer of particles (actually a string since the suspension is two-dimensional) subjected to a bulk linear shear flow. Hydrodynamic interactions with neighbouring layers will be neglected. However, electrostatic forces due to the presence of these neighbouring layers will be included in the analysis as they are believed to be responsible for stabilizing the particle layers. We further assume that the hydrodynamic force on each particle is equal to the force that would exist if that particle were alone in the fluid, plus contributions due to lubrication interactions with its two nearest neighbours in the layer. Finally, since our simulations indicate that the loss of microstructural order is due to the formation of particle doublets in the suspension, we will assume that positions and velocities of the ith and $(i+2)$th particles in the layer are related by

$$\left.\begin{aligned} x_{i+2} &= x_i + 2R_0, \quad y_{i+2} = y_i, \\ \boldsymbol{u}_{i+2} &= \boldsymbol{u}_i, \quad \boldsymbol{\omega}_{i+2} = \boldsymbol{\omega}_i, \end{aligned}\right\} \tag{10}$$

where x denotes streamwise position, y denotes cross-stream position, $\boldsymbol{u}$ denotes translational velocity, $\boldsymbol{\omega}$ denotes rotational velocity, and R_0 is set to $(\pi/\phi_a)^{1/2}$ for consistency with the simulations. Therefore, the stability of the layer is completely determined by the stability of a two-particle configuration within the layer. The two particles in this configuration are labelled 1 and 2 and are shown in figure 11.

With the above assumptions, and assuming that the fluid motion is described by Stokes equations, the hydrodynamic forces and torques on particles 1 and 2 can be expressed as

$$\begin{pmatrix} \boldsymbol{F}_{h1} \\ \boldsymbol{F}_{h2} \\ \boldsymbol{T}_{h1} \\ \boldsymbol{T}_{h2} \end{pmatrix} = -\begin{pmatrix} \boldsymbol{A}^{11} & \boldsymbol{A}^{10}+\boldsymbol{A}^{12} & \tilde{\boldsymbol{B}}^{11} & \tilde{\boldsymbol{B}}^{10}+\tilde{\boldsymbol{B}}^{12} \\ \boldsymbol{A}^{21}+\boldsymbol{A}^{23} & \boldsymbol{A}^{22} & \tilde{\boldsymbol{B}}^{21}+\tilde{\boldsymbol{B}}^{23} & \tilde{\boldsymbol{B}}^{22} \\ \boldsymbol{B}^{11} & \boldsymbol{B}^{10}+\boldsymbol{B}^{12} & \boldsymbol{C}^{11} & \boldsymbol{C}^{10}+\boldsymbol{C}^{12} \\ \boldsymbol{B}^{21}+\boldsymbol{B}^{23} & \boldsymbol{B}^{22} & \boldsymbol{C}^{21}+\boldsymbol{C}^{23} & \boldsymbol{C}^{22} \end{pmatrix} \cdot \begin{pmatrix} \boldsymbol{u}_1-\boldsymbol{u}_1^{\infty} \\ \boldsymbol{u}_2-\boldsymbol{u}_2^{\infty} \\ \boldsymbol{\omega}_1-\boldsymbol{\omega}^{\infty} \\ \boldsymbol{\omega}_2-\boldsymbol{\omega}^{\infty} \end{pmatrix}$$
$$+ \begin{pmatrix} \tilde{\boldsymbol{G}}^{10} & \tilde{\boldsymbol{G}}^{11} & \tilde{\boldsymbol{G}}^{12} & \boldsymbol{0} \\ \boldsymbol{0} & \tilde{\boldsymbol{G}}^{21} & \tilde{\boldsymbol{G}}^{22} & \tilde{\boldsymbol{G}}^{23} \\ \tilde{\boldsymbol{H}}^{10} & \tilde{\boldsymbol{H}}^{11} & \boldsymbol{H}^{12} & \boldsymbol{0} \\ \boldsymbol{0} & \tilde{\boldsymbol{H}}^{21} & \tilde{\boldsymbol{H}}^{22} & \tilde{\boldsymbol{H}}^{23} \end{pmatrix} : \begin{pmatrix} \boldsymbol{e}^{\infty} \\ \boldsymbol{e}^{\infty} \\ \boldsymbol{e}^{\infty} \\ \boldsymbol{e}^{\infty} \end{pmatrix}, \tag{11}$$

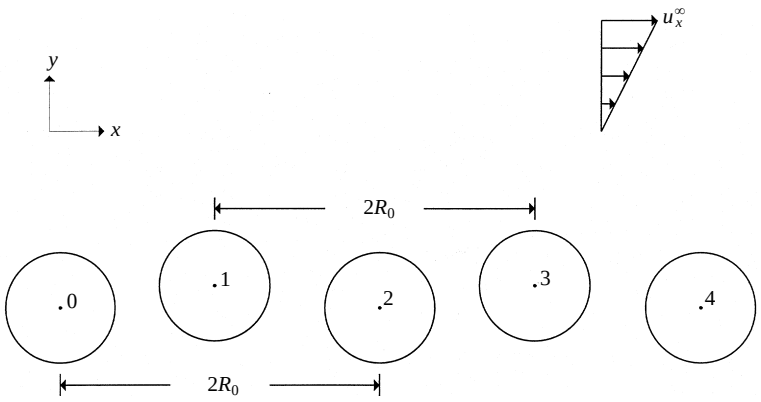

FIGURE 11. Single-layer geometry used for the linear stability analysis. Particle positions are assumed periodic, with cross-stream positions of particles i and $i+2$ equal and their streamwise positions differing by $2R_0$. Particles are suspended in a Newtonian liquid subjected to a bulk linear shear flow. $R_0 = (\pi/\phi_a)^{1/2}$, $\phi_a = 0.74$.

where $\boldsymbol{F}_{h_i}$ is the hydrodynamic force exerted on the ith particle $\boldsymbol{T}_{h_i}$ is the hydrodynamic torque exerted on the ith particle, $\boldsymbol{u}_i$ is the translational velocity of the ith particle, $\boldsymbol{\omega}_i$ is the rotational velocity of the ith particle, $\boldsymbol{u}_i^\infty$ is the translational velocity of the bulk flow that would exist at the centre of the ith particle if the particles were absent, $\boldsymbol{\omega}^\infty$ is the rotational velocity of the bulk flow that would exist if the particles were absent, and $\boldsymbol{e}^\infty$ is the bulk rate of strain tensor that would exist in the absence of the particles. For the assumed bulk flow, e_{xy} and e_{yx} are the only non-zero components of $\boldsymbol{e}^\infty$. The matrix elements, which we denote more generally as $\boldsymbol{P}^{\alpha\beta}$, are resistance tensors that relate the relative translational or rotational motion of particle β to the force or torque exerted on particle α. In (11), all quantities have been non-dimensionalized as described in §2. Consistent with this scheme, the resistance tensors have been scaled by $6\pi\eta_s a^l$, with $l = 1$ for the $\boldsymbol{A}$ tensors, $l = 2$ for the $\boldsymbol{B}$, $\tilde{\boldsymbol{B}}$, and $\tilde{\boldsymbol{G}}$ tensors, and $l = 3$ for the $\boldsymbol{C}$, and $\tilde{\boldsymbol{H}}$ tensors. These resistance tensors are adaptations of quantities presented in Kim & Karrila (1991), with a correction given by Ladd (1990). Detailed expressions for these tensors are available from the JFM editorial office. Because of the two-dimensional geometry, forces and translational velocities are restricted to the (x, y)-plane while torques and rotational velocities are restricted to the z-direction.

As described in §2, the particles are assumed to be charge-stabilized with electrostatic forces well-described by the constant-potential Derjaguin formula (Russel *et al.* 1989). For interactions between particles within the layer, electrostatic forces are given by equation (6). However, since particles in the layered configurations are separated by a gap of about 0.06 when $\phi_a = 0.74$, the second term in (6) is neglected.

Electrostatic forces exerted on particles in the layer by particles in adjacent layers will fluctuate in time due to the shear-induced relative motion of these layers. The time scale of these fluctuations is approximately unity. However, as can be seen in figure 6, the time required for an ordered configuration to completely disorder is relatively large, ranging from about 300 dimensionless time units for $\dot{\gamma} = 12\ \mathrm{s}^{-1}$ to about 50 dimensionless time units for $\dot{\gamma} = 100\ \mathrm{s}^{-1}$. Therefore, we will assume that the effect of these fluctuating electrostatic forces on the long-time behaviour of particles 1 and 2 is the same as the effect of their time averages. To compute these averages, we assume that the two nearest adjacent layers of particles (which are the only layers that contribute significantly to the electrostatic forces exerted on particles 1 and 2) are at

constant cross-stream positions $y = \pm R_0$, that these layers move with constant velocities equal to the bulk velocity at their respective cross-stream positions, that the particles within the layers are evenly spaced in the streamwise direction, and that the positions of particles 1 and 2 vary slowly in comparison with the time scale of the force fluctuations. With these assumptions, the electrostatic forces exerted on particles 1 and 2 by the adjacent layers are approximately time periodic. Therefore, the time averages of these forces can be computed by integration over one fluctuation period. Subject to these conditions, the y-component of the time-averaged electrostatic force due to the adjacent layer at $y = R_0$ can be written

$$\frac{1}{\dot{\gamma}^* R_0} \int_{-R_0/2}^{R_0/2} \frac{\tau \exp(-\tau h)}{1+\exp(-\tau h)} \frac{y' - R_0}{(x^2 + (y' - R_0)^2)^{1/2}} \mathrm{d}x, \tag{12}$$

where the time average has been replaced by a spatial average due to the constant velocity of the adjacent layer, $(0, y')$ is the position of particle 1 (or 2), (x, R_0) is the position of the only particle in the adjacent row contributing significantly to the integral, and $h = (x^2 + (y' - R_0)^2)^{1/2} - 2$. The x-component of the time-averaged force is identically zero. Employing similar arguments, the y-component of the time-averaged force arising from the adjacent row at $y = -R_0$ can be written

$$\frac{-1}{\dot{\gamma}^* R_0} \int_{-R_0/2}^{R_0/2} g(x, -y') \, \mathrm{d}x, \tag{13}$$

where $g(x, y')$ is the integrand in (12). Expanding the integrals in (12) and (13) in Taylor series about $y' = 0$, and combining, leads to

$$\frac{2}{\dot{\gamma}^*} \left[\frac{y'}{R_0} \int_{-R_0/2}^{R_0/2} g_y(x, 0) \, \mathrm{d}x + O(y'^3) \right], \tag{14}$$

which is the y-component of the time-averaged electrostatic force exerted on particle 1 (or 2) due to the presence of both adjacent layers of particles. Taking $\tau = 47.656$ and $R_0 = (\pi/0.74)^{1/2}$ for consistency with the simulations, numerical integration of the integral in (14) yields $-29.653\,358 R_0$. The $O(y'^3)$ term in (14) is not required since the stability analysis is linear.

As in the simulations, particles are assumed to be force- and torque-free. Therefore, the equations governing the motion of particles 1 and 2 are

$$\frac{\mathrm{d}\hat{x}_i}{\mathrm{d}t} = \hat{u}_i, \tag{15}$$

for $i = 1, \ldots, 4$, where $\hat{\boldsymbol{x}} = (x_1, y_1, x_2, y_2)^T$ and $\hat{\boldsymbol{u}} = (u_{1x}, u_{1y}, u_{2x}, u_{2y})^T$. Since the particles are spherical, angular positions are neglected in the stability analysis. With equation (11) written more compactly as

$$\hat{F}_{h_i} = -R_{ij} \Delta u_j + B_i, \tag{16}$$

the components of $\hat{\boldsymbol{u}}$ can be obtained from

$$\hat{u}_i = \hat{u}_i^{\infty} + R_{ij}^{-1} (B_j + \hat{F}_{p_j}). \tag{17}$$

In (17), $\hat{F}_{p_j}$ contains the electrostatic forces exerted on particles 1 and 2, and $\hat{\boldsymbol{u}}^{\infty} = (y_1, 0, y_2, 0)^T$ for the assumed bulk linear shear flow.

To determine the stability of solutions of equation (15), we employ standard techniques. Solutions of the form $\hat{x}_{b_i} + \hat{x}_i'$ are assumed to exist, where $\hat{x}_{b_i}$ is the base-

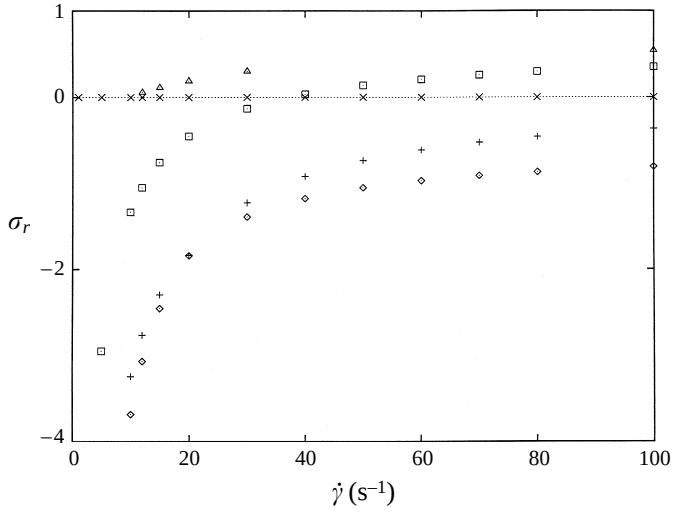

FIGURE 12. Real parts of eigenvalues σ_r obtained from a linear stability analysis of a single layer of uniformly spaced particles at $y = 0$. $R_0 = (\pi/\phi_a)^{1/2}$, $\phi_a = 0.74$, $\tau = 47.656$. $\diamond$, Mode 1; $+$, mode 2; $\boxdot$, mode 3; $\times$, mode 4. For comparison, growth rates associated with the Δy_D shown in figure 8 are also shown ($\triangle$).

state solution, the stability of which is of interest, and $\hat{x}_i'$ is a small perturbation. Substituting $\hat{x}_{b_i} + \hat{x}_i'$ into equation (15) and linearizing yields

$$\frac{\mathrm{d}\hat{x}_i'}{\mathrm{d}t} = \left(\frac{\partial \hat{u}_i}{\partial \hat{x}_j}\right)_{\hat{\boldsymbol{x}}_b} \hat{x}_j', \tag{18}$$

which is a fourth-order system of linear ordinary differential equations. Furthermore, because of the neglect of hydrodynamic interactions with adjacent particle layers and the time averaging of electrostatic forces associated with these layers, the coefficient matrix $(\partial \hat{u}_i/\partial \hat{x}_j)_{\hat{\boldsymbol{x}}_b}$ is time independent. Therefore, solutions of equation (18) have the form

$$\hat{x}_i' = b_i \mathrm{e}^{\sigma t}, \tag{19}$$

where σ is an eigenvalue of the coefficient matrix and b_i is its associated eigenvector. For this work, the coefficient matrix and its eigen pairs were computed using *Mathematica* (Wolfram 1991).

For the stability computations, we assume that particles in the layer are uniformly spaced and located at $y = 0$. Therefore, we take the base-state positions of particles 1 and 2 to be $\hat{\boldsymbol{x}}_b = (0, 0, R_0, 0)^T$. Consistent with the simulations, $R_0 = (\pi/0.74)^{1/2}$, $\tau = 47.656$, and $\dot{\gamma}^* = 0.6575\dot{\gamma}$. For this base state, eigenvalues and eigenvectors of the coefficient matrix have been computed for shear rates in the range $1 \leqslant \dot{\gamma} \leqslant 100$ s^{-1}. For all four modes the eigenvalues are real and simple, with σ_r shown as a function of shear rate in figure 12. For the entire range of $\dot{\gamma}$ shown, one mode is neutrally stable. The other three modes are stable at low shear rate, but become less stable as the shear rate is increased. The least stable mode becomes unstable at $\dot{\gamma} \approx 40$ s^{-1} ($\dot{\gamma}^* \approx 26.3$), indicating that the simplified microstructure we have considered is indeed subject to a linear instability. In the simulations, the critical shear rate was between 10 and 12 s^{-1}. Growth rates associated with the Δy_D shown in figure 8 are also shown in figure 12 and are in good qualitative agreement with the stability predictions.

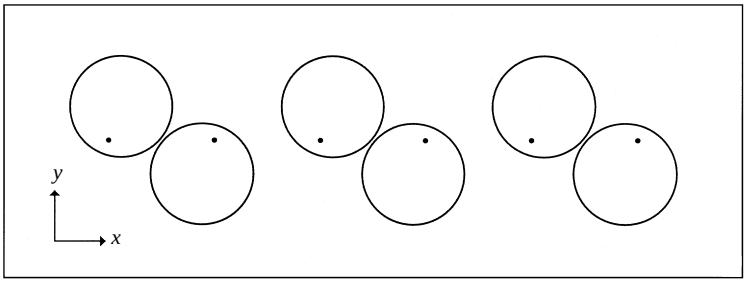

FIGURE 13. Layer of uniformly spaced particles at $y = 0$ that has been perturbed by the eigenvector of the most unstable mode (mode 3). The norm of the eigenvector is unity. $\dot{\gamma} = 100\ \mathrm{s}^{-1}$, $R_0 = (\pi/\phi_a)^{1/2}$, $\phi_a = 0.74$, $\tau = 47.656$. The dots mark the centres of the unperturbed particles. For clarity, the periodicity of the two-particle configuration has been shown.

In figure 13, we show a layer of particles in the base state that has been perturbed by the eigenvector of the most unstable mode. For the configuration shown, $\dot{\gamma} = 100\ \mathrm{s}^{-1}$. The effect of this mode is to displace the upstream member of a particle pair in the positive x- and y-directions, i.e. downstream and upwards, and to displace the downstream member of a pair an equal amount in the negative $x-$ and y-directions. For perturbations of this type, the mean shear will tend to increase the magnitudes of the x-components of the perturbation. In addition, since the perturbed row of particles is not evenly spaced, lubrication forces exerted by adjacent particles will be unbalanced and will tend to increase the magnitudes of both the x- and y-components of the perturbation. The primary effect of repulsion is expected to be stabilizing. As a result, for sufficiently high shear rates, perturbations of the type shown in figure 13 are expected to be unstable, with the mechanism for this instability as outlined above. In addition, the perturbed layer contains doublets similar to those seen in the simulations.

As a check on our stability computations, the coefficient matrix was also computed using fourth-order finite differences. The velocity vectors needed for the difference equations were obtained using a version of our Stokesian Dynamics code, modified so that the hydrodynamic and repulsive forces were computed exactly as described in this section. Eigen pairs of the coefficient matrix were computed using a LAPACK routine (Anderson *et al.* 1992) that employed QR iteration. With $\Delta\hat{x}_j = 10^{-4}$, elements of the coefficient matrix, eigenvalues, and eigenvectors all differed by less than 10^{-10}, in relative terms, from analogous quantities computed using *Mathematica*.

Finally, we comment on the generalization of our results to other systems. For the suspension considered here, its behaviour is controlled by three dimensionless parameters; τ, ϕ_a and $\dot{\gamma}^*$. Therefore, for fixed τ and ϕ_a, the dimensionless critical shear rate, i.e. $\dot{\gamma}_c^*$, should be invariant. An examination of $\dot{\gamma}_c^*$ indicates that the dimensional critical shear rate $\dot{\gamma}_c$ as predicted by the simulations or the stability analysis should be proportional to ϵ, ψ_0^2, $1/\eta_s$, and $1/a^2$. Furthermore, since the suspensions becomes more hard-sphere like with increasing τ, we expect $\dot{\gamma}_c$ to vary inversely with this parameter. Finally, since hydrodynamic interactions are singular at contact but electrostatic forces are finite, we expect $\dot{\gamma}_c$ to decrease with increasing concentration. These conjectures are consistent with the findings of others (see e.g. Hoffman 1974 and Barnes 1989).

3.4. *Influence of system size*

As noted by Bossis & Brady (1984), the computational cost of Stokesian Dynamics scales as $O(N^3)$. Therefore, simulations are impractical for all but modest system sizes, and may exhibit some dependence on the number of particles employed. To assess this

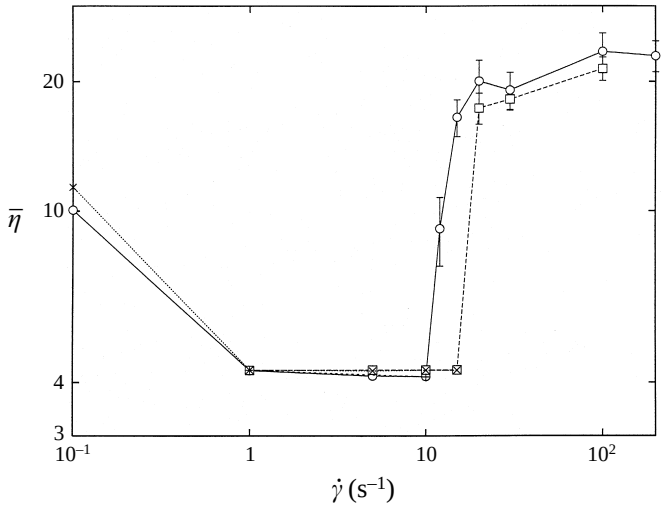

FIGURE 14. Relative viscosity $\bar{\eta}$ as a function of shear rate $\dot{\gamma}$ for Φ, $N = 25$; Φ, $N = 26$; $+$, $N = 81$; $\times$, $N = 100$, obtained from Stokesian Dynamics simulations of a monolayer suspension of charge-stabilized rigid spheres in a bulk linear shear flow. For $N = 25$ and $\dot{\gamma} \geqslant 12\ \mathrm{s}^{-1}$, and $N = 36$ and $\dot{\gamma} \geqslant 20\ \mathrm{s}^{-1}$, additional repulsion with $\tau_1 = 10^6$ and $\dot{\gamma}_1^* = 1$ was used to prevent overlapping particles. For $N = 81$ and 100, additional repulsion was not employed since $\bar{\eta}$ is shown for ordered suspensions only. Error bars are omitted when smaller than the symbol. $\phi_a = 0.74$, $\tau = 47.656$.

dependence for our results, a number of the simulations discussed in §§ 3.1 and 3.2, for which $N = 25$, have been repeated with $N = 36$, 81 and 100. Other than the number of particles N and the domain size h_{cell}, which varied due to the variation of N, all numerical parameters were identical to those employed in the $N = 25$ simulations discussed previously.

The influence of system size on the bulk viscosity $\bar{\eta}$ is illustrated in figure 14, where the shear-rate dependence of $\bar{\eta}$ is shown for $N = 25$, 36, 81 and 100. Viscosities for $N = 25$ were shown previously in figure 3. In addition, for $N = 81$ and 100 computational costs precluded performing simulations at supercritical shear rates. For all shear rates shown, $\bar{\eta}$ shows little variation with system size. Just prior to the onset of shear thickening $\bar{\eta} \approx 4$, while $\bar{\eta}$ is near 20 for $\dot{\gamma} \geqslant 20\ \mathrm{s}^{-1}$. The critical shear rate $\dot{\gamma}_c$ does exhibit a weak dependence on N, with $10 < \dot{\gamma}_c \leqslant 12$ for $N = 25$ and $15 < \dot{\gamma}_c \leqslant 20$ for $N = 36$. In addition, $\dot{\gamma}_c$ exhibits some dependence on the shear rate history. For $N = 36$ and 100, the suspension disordered at $\dot{\gamma} = 10\ \mathrm{s}^{-1}$ when simulations were initiated with configurations obtained from $\dot{\gamma} = 1\ \mathrm{s}^{-1}$ simulations. However, when initiated with configurations obtained from $\dot{\gamma} = 5\ \mathrm{s}^{-1}$ simulations, the suspension remained ordered at $\dot{\gamma} = 10\ \mathrm{s}^{-1}$, suggesting metastability at this shear rate. Similar behaviour was not observed for $N = 25$, with the asymptotic microstructure at $\dot{\gamma} = 10\ \mathrm{s}^{-1}$ consisting of ordered layers even for simulations initiated with disordered configurations. This suggests stability with respect to both infinitesimal and finite-amplitude disturbances. Despite these discrepancies, system size does not appear to have a large effect on the bulk viscosity. The microstructure, as quantified by $g(y)$, also shows little variation with N.

In agreement with our $N = 25$ results the onset of disorder in simulations employing 36, 81 and 100 particles also appears to be due to a linear instability that leads to the formation of particle doublets in the suspension. This is demonstrated in figures 15 and 16. In figure 15, typical particle configurations for an initially ordered suspension

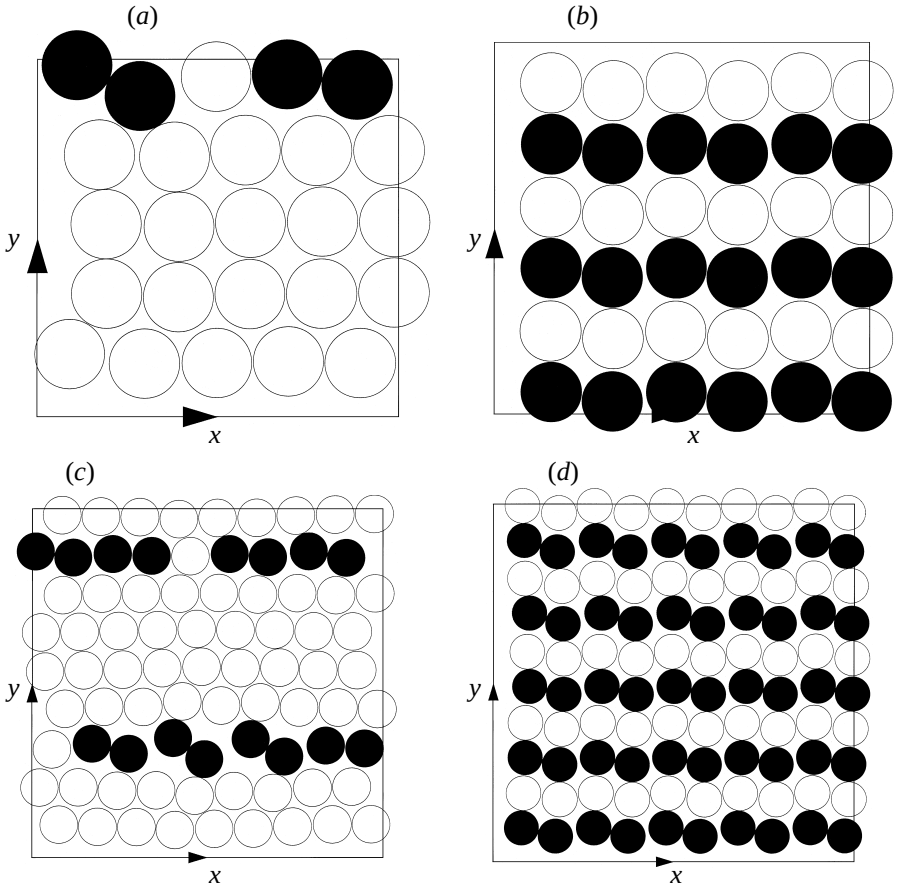

FIGURE 15. Comparison of instantaneous particle configurations for different values of N, obtained from Stokesian Dynamics simulation of a monolayer suspension of charge-stabilized rigid spheres in a bulk linear shear flow. For $N = 25$ and 81, initial configurations were obtained from subcritical simulations for which $\dot{\gamma} = 10\ \mathrm{s}^{-1}$. For $N = 36$ and 100, initial configurations were obtained from subcritical simulations for which $\dot{\gamma} = 15\ \mathrm{s}^{-1}$. Flow is from left to right. Particle doublets are identified by shading. $\phi_a = 0.74$, $\tau = 47.656$, $\dot{\gamma} = 20\ \mathrm{s}^{-1}$. (*a*) $N = 25$, $t = 124$; (*b*) $N = 36$, $t = 30$; (*c*) $N = 81$, $t = 118$; (*d*) $N = 100$, $t = 41$.

undergoing supercritical shearing are shown for $N = 25$, 36, 81 and 100. Initial configurations for these simulations were obtained from simulations at the highest shear rate for which the sliding layer microstructure was maintained: $\dot{\gamma} = 10\ \mathrm{s}^{-1}$ for $N = 25$ and 81, and $\dot{\gamma} = 15\ \mathrm{s}^{-1}$ for $N = 36$ and 100. For the configurations shown, $\dot{\gamma} = 20\ \mathrm{s}^{-1}$. Qualitatively these configurations are quite similar, with particle doublets (identified by the black shading) observed for all four values of N. These doublets rotate due to the imposed flow and eventually disrupt the microstructural order of the suspension. However, distinct quantitative differences in configurations are also observed. For $N = 25$ and 81, only one or two rows of particles appear to contain doublets. In contrast, for $N = 36$ and 100, doublets are present in every other row. These differences are clearly due to system size since the alternating pattern of doublets observed for $N = 36$ and 100 is incompatible with the imposed periodic boundary conditions and the odd number of rows in configurations containing 25 and 81 particles. In addition, although the rows of unshaded particles in figures 15(*b*) and 15(*d*) do appear to contain doublets, these particle pairs do not exhibit consistent

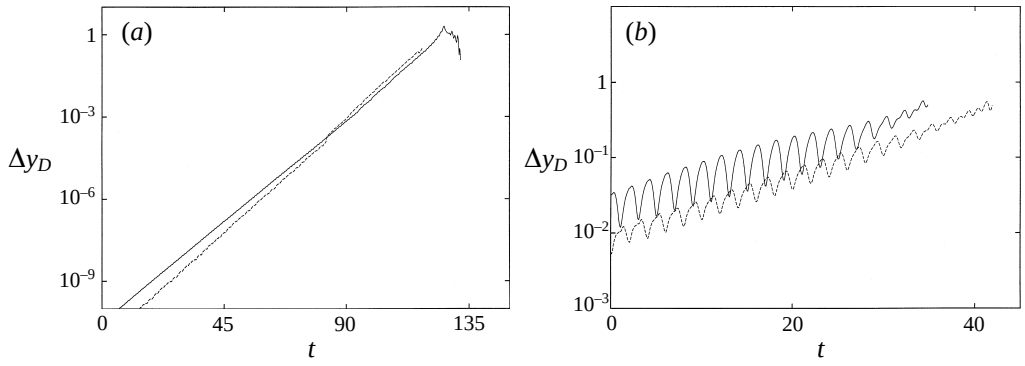

FIGURE 16. Temporal dependence of cross-stream separation distance Δy_D between particle centres in a typical doublet. For $N = 25$ and 81, initial configurations were obtained from subcritical simulations for which $\dot{\gamma} = 10\ \mathrm{s}^{-1}$. For $N = 36$ and 100, initial configurations were obtained from subcritical simulations for which $\dot{\gamma} = 15\ \mathrm{s}^{-1}$. $\dot{\gamma} = 20\ \mathrm{s}^{-1}$, $\phi_a = 0.74$, $\tau = 47.656$. (*a*) $N = 25$ (——) and $N = 81$ (– – – –), (*b*) $N = 36$ (——) and $N = 100$ (-----).

clockwise rotation and are therefore not considered to be doublets. Instead, these particle pairs rotate in both directions in response to the relative motion of adjacent layers.

The temporal evolution of Δy_D associated with doublets shown in figure 15 is shown in figure 16. For all values of N, Δy_D exhibits exponential growth, suggesting that the temporal evolution of doublets when $N = 36$, 81 and 100 is also governed by a linear instability of the layered configurations. However, despite these similarities, the time evolution of Δy_D does vary with system size. In particular, the evolution of Δy_D when $N = 25$ and 81 is significantly different from observed behaviour when $N = 36$ and 100. For $N = 25$ and 81, Δy_D is initially quite small, $O(10^{-10})$, but grows exponentially until the suspension begins to exhibit a significant amount of disorder, which it does when $\Delta y_D = O(1)$. Exponential growth of Δy_D, on average, is also observed for $N = 36$ and 100. However, in contrast to the $N = 25$ and 81 results, Δy_D is initially quite large, $O(10^{-2})$, and exhibits considerable oscillation. We attribute these differences to the configurations used to initiate the simulations, and to microstructural differences that arise once the doublets begin to form. For all four values of N, initial conditions consisted of sliding layer configurations obtained from simulations at subcritical shear rates. For $N = 25$ and 81, particles in each layer of the initial configuration were in almost perfect alignment. As a result, when these configurations were used to initiate simulations at supercritical shear rates, initial values of Δy_D were also quite small. For $N = 36$ and 100, particles in the initial configurations formed alternating patterns of doublets similar to those seen in figures 15(*b*) and 15(*d*), with particles in these doublets offset by approximately 1 %. As a result, when these configurations were used to initiate simulations at supercritical shear rates, initial values of Δy_D were also about 1 %. Oscillations in Δy_D when $N = 36$ and 100 are believed to be due to interactions between doublets and adjacent layers of particles, which are closer together than when $N = 25$ and 81 because of the alternating pattern of doublets.

In a small number of cases, the variation of Δy_D deviated from the behaviour observed in figure 16. As noted in §3.2, doublets were intermittently present for $\dot{\gamma} = 10\ \mathrm{s}^{-1}$ when $N = 25$ but did not cause the suspension to disorder. However, when configurations containing these doublets were used to initiate simulations at supercritical shear rates, the variation of Δy_D was similar to the variation observed in figure 16(*b*), not figure 16(*a*). For $N = 36$, some configurations for $\dot{\gamma} = 15\ \mathrm{s}^{-1}$ did not

contain doublets. As a result, when configurations such as these were used to initiate simulations at supercritical shear rates, the onset of disorder was delayed significantly. However, in all cases exponential growth of Δy_D was observed.

The results discussed above illustrate the non-trivial influence of system size for simulations employing a small number of particles. However, despite the obvious effect of N on various aspects of our results, the basic mechanism responsible for the onset of disorder in our simulations appears to be the same for all values of N used. Therefore, we believe our results are likely to be in qualitative agreement with results obtained in the limit $N \to \infty$.

Finally, we note that for all of our reported results, N was a perfect square (25, 36, 81 or 100). Since our computational domain was square prior to shear, this choice of N facilitates the formation of particle layers. For simulations in which the number of particles is not a perfect square, the formation of layers is inhibited to some degree. However, since experimental studies (see e.g. Hoffman 1972) have established that monodisperse charge- and sterically stabilized suspensions exhibit a sliding layer microstructure prior to the onset of shear thickening, our simulations were designed to mimic this behaviour, with N chosen to facilitate layer formation.

4. Conclusions

Stokesian Dynamics has been used to investigate the origins of shear thickening in monodisperse charge-stabilized colloidal suspensions. In agreement with established experimental data for these types of suspensions (see e.g. Hoffman 1972; Chow & Zukoski 1995*b*; Chen *et al*. 1994), our results indicate that shear thickening is associated with an order–disorder transition of the suspension microstructure. Below the critical shear rate at which this transition occurs, the suspension microstructure consists of two-dimensional analogues of experimentally observed sliding layer configurations. Above this critical shear rate, suspensions are disordered and exhibit viscosities and microstructures characteristic of suspensions of non-Brownian hard spheres. This suggests that shear thickening in monodisperse charge-stabilized suspensions, and the associated loss of microstructural order, are manifestations of a transition to a high-shear regime in which charge-stabilized suspensions become rheologically and microstructurally indistinguishable from suspensions of non-Brownian hard spheres.

In agreement with other investigations (see e.g. D'Haene *et al*. 1993; Phung *et al*. 1996; Bender & Wagner 1996), the high viscosity that defines shear thickening is evidently due to the formation of large particle clusters. These clusters can generate high stresses due to the thin lubrication layers between particles. However, a key difference between the shear thickening observed here and the shear thickening observed in hard-sphere systems appears to be the mechanism leading to the cluster-dominated regime. For monodisperse charge-stabilized systems with particles moving in ordered layers, this study shows that an instability causes the order–disorder transition which leads to conditions under which particle clusters can form. In other words, the order–disorder transition does not cause the shear thickening *per se*, but it sets up the conditions under which particle clusters can form and cause shear thickening.

Our results further suggest that the observed transition from ordered layers to an amorphous microstructure is due to the formation of doublets in which the component particles are offset in the shear-gradient direction and separated by less than the average spacing within the ordered layers. These doublets tend to rotate due to the

applied shear and disrupt long-range microstructural order. Examination of the cross-stream dimension of these doublets indicates exponential growth, suggesting that the evolution of these doublets is due to a linear instability of the sliding layer microstructure. These findings are consistent with the instability mechanism first advanced by Hoffman (1974). However, our results are the first concrete evidence in support of this view.

Our contention that the observed doublets are a manifestation of a microstructural instability is supported by results of a linear stability analysis. Results of this analysis indicate that a single string of charge-stabilized particles subjected to a bulk linear shear flow, with the particles identical in all respects to the particles in the simulations, becomes linearly unstable above a shear rate of about $40\ s^{-1}$. The mechanism responsible for this instability appears to be the combined effects of the mean shear and lubrication forces acting on the perturbed configuration. This instability leads to the formation of particle doublets similar to those observed in the simulations.

Since particles in our simulations are force- and torque-free, the results clearly indicate that a force or torque imbalance is not a necessary condition for the observed instability, microstructural disorder, or shear thickening. This finding is consistent with the well-established view that particle inertia is negligible in colloidal suspensions subjected to moderate rates of deformation.

A body of existing work indicates that in some colloidal suspensions, an order–disorder transition is neither necessary nor sufficient for the occurrence of shear thickening. For example, hard-sphere (see e.g. D'Haene *et al.* 1993; Phung *et al.* 1996; Bender & Wagner 1996) and polydisperse suspensions (see e.g. Laun *et al.* 1992) are believed to shear thicken in the absence of an order–disorder transition. Furthermore, even when suspended particles are repulsive and relatively monodisperse, moderately dense suspensions will disorder without shear thickening (see e.g. Chow & Zukoski 1995*b*). However, the results discussed here are for a very dense monodisperse charge-stabilized suspension, for which the link between order–disorder transitions and shear thickening is well established. Thus our results are consistent with the findings of other investigations.

Results obtained for a range of system sizes are in qualitative agreement, suggesting our findings are likely to be qualitatively consistent with results obtained using a very large number of particles. However, quantitative differences between results obtained with different values of N illustrate the sensitivity of simulations of ordered suspensions to variations in system size when N is small. Clearly, there is a need to develop methods that will allow simulations of much larger systems.

Our results do not include the effect of Brownian motion. The critical Péclet number $Pe = 6\pi\eta_s a^3\dot{\gamma}/kT$ for our simulations was about 3400 (based on the physical parameters of Boersma *et al.*'s experiments). Therefore, even at the high densities considered, we believe it is reasonable to assume that Brownian motion is of secondary importance.

Owing to computational constraints, our simulations were limited almost entirely to monolayer suspensions. To gain a better and more quantitative understanding of microstructural transitions and shear thickening in real systems, simulations of three-dimensional suspensions should be performed. While we would not expect our findings to change significantly with the inclusion of three-dimensionality, various aspects of the results, such as critical shear rates for the onset of disorder, could be quite different. We note that with current methodologies, three-dimensional Stokesian Dynamics simulations are expensive and impractical for routine use.

Although the current work has included an analysis of microstructural stability, this

analysis was limited to a relatively simple one-dimensional microstructure (i.e. a single string of particles). Future work in this area should include analysis aimed at predicting the stability of more realistic two-dimensional microstructures, such as those in our simulations. Such an analysis could be readily performed using the Stokesian Dynamics methodology in combination with Floquet theory. In addition to answering fundamental questions regarding the nature of observed microstructural transitions, stability analysis could provide the theoretical foundation for a computational tool for estimating critical shear rates in monodisperse, repulsive suspensions.

The authors wish to thank Professor J. F. Brady for the use of his Stokesian Dynamics simulation code and Dr Nancy Huang of the Chinese Academy of Sciences for her help in the initial programming stages of this work. Financial support for this work has been provided by the Monsanto Company and the University of Illinois. Computations described herein were performed on an IBM RS/6000 workstation provided through the IBM Shared University Research program.

REFERENCES

Allen, M. P. & Tildesley, D. J. 1987 *Computer Simulation of Liquids*. Clarendon.

Anderson, E., Bai, Z., Bischof, C., Demmel, J., Dongarra, J., Du Croz, J., Greenbaum, A., Hammarling, S., McKenney, A., Ostrouchov, S. & Sorensen, D. 1992 *LAPACK Users' Guide*. SIAM.

Barnes, H. A. 1989 Shear-thickening ('dilatancy') in suspensions of nonaggregating solid particles dispersed in Newtonian liquids. *J. Rheol.* **33**, 329–366.

Bendat, J. S. & Persol, A. G. 1986 *Random Data: Analysis and Measurement Procedures*. John Wiley and Sons.

Bender, J. & Wagner, N. J. 1996 Reversible shear thickening in monodisperse and bidisperse colloidal dispersions. *J. Rheol.* **40**, 899–916.

Boersma, W. H., Baets, P. J. M., Laven, J. & Stein, H. N. 1991 Time-dependent behavior and wall slip in concentrated shear thickening dispersions. *J. Rheol.* **35**, 1093–1120.

Boersma, W. H., Laven, J. & Stein, H. N. 1990 Shear thickening (dilatancy) in concentrated dispersions. *AICHE J.* **36**, 321–332.

Boersma, W. H., Laven, J. & Stein, H. N. 1995 Computer simulations of shear thickening of concentrated dispersions. *J. Rheol.* **39**, 841–860.

Bonnecaze, R. T. & Brady, J. F. 1992 Dynamic simulation of an electrorheological fluid. *J. Chem. Phys.* **96**, 2183–2202.

Bossis, G. & Brady, J. F. 1984 Dynamic simulation of sheared suspensions. I. General method. *J. Chem. Phys.* **80**, 5141–5154.

Bossis, G. & Brady, J. F. 1989 The rheology of Brownian suspensions. *J. Chem. Phys.* **91**, 1866–1874.

Brady, J. F. & Bossis, G. 1985 The rheology of concentrated suspensions of spheres in simple shear flow by numerical simulation. *J. Fluid Mech.* **155**, 105–129.

Brady, J. F. & Bossis, G. 1988 Stokesian dynamics. *Ann. Rev. Fluid Mech.* **20**, 111–157.

Brady, J. F., Phillips, R. J., Lester, J. C. & Bossis, G. 1988 Dynamic simulation of hydrodynamically interacting suspensions. *J. Fluid Mech.* **195**, 257–280.

Chaffey, C. E. & Wagstaff, I. 1977 Shear thinning and thickening rheology. II. Volume fraction and size of dispersed particles. *J. Colloid Interface Sci.* **59**, 63–75.

Chang, C. & Powell, R. L. 1993 Dynamic simulation of bimodal suspensions of hydrodynamically interacting spherical particles. *J. Fluid Mech.* **253**, 1–25.

Chen, L. B., Chow, M. K., Ackerson, B. J. & Zukoski, C. F. 1994 Rheological and microstructural transitions in colloidal crystal. *Langmuir* **10**, 2817–2829.

Chow, M. K. & Zukoski, C. F. 1995*a* Gap size and shear history dependencies in shear thickening of a suspension ordered at rest. *J. Rheol.* **39**, 15–32.

Chow, M. K. & Zukoski, C. F. 1995*b* Nonequilibrium behavior of dense suspensions of uniform particles: Volume fraction and size dependence of rheology and microstructure. *J. Rheol.* **39**, 33–59.

Conte, S. D. & Boor, C. de 1980 *Elementary Numerical Methods: An Algorithmic Approach*. McGraw-Hill.

D'Haene, P., Mewis, J. & Fuller, G. G. 1993 Scattering dichroism measurements of flow-induced structure of a shear thickening suspension. *J. Colloid Interface Sci.* **156**, 350–358.

Dratler, D. I. & Schowalter, W. R. 1996 Dynamic simulation of suspensions of non-Brownian hard spheres. *J. Fluid Mech.* **325**, 53–77.

Durlofsky, L., Brady, J. F. & Bossis, G. 1987 Dynamic simulation of hydrodynamically interacting particles. *J. Fluid Mech.* **180**, 21–49.

Hoffman, R. L. 1972 Discontinuous and dilatant viscosity behavior in concentrated suspensions. I. Observation of flow instability. *Trans. Soc. Rheol.* **16**, 155–173.

Hoffman, R. L. 1974 Discontinuous and dilatant viscosity behavior in concentrated suspensions. II. Theory and experimental tests. *J. Colloid Interface Sci.* **46**, 491–506.

Hoffman, R. L. 1991 Interrelationships of particle structure and flow in concentrated suspensions. *Mater. Res. Soc. Bull.* **16**, 32–37.

Kim, S. & Karrila, S. J. 1991 *Microhydrodynamics: Principles and Selected Applications*. Butterworth-Hiemann.

Ladd, A. J. C. 1990 Hydrodynamic transport coefficients of random dispersions of hard spheres. *J. Chem. Phys.* **93**, 3484–3494.

Laun, H. M., Bung, R., Hess, S., Loose, W., Hess, O., Hahn, K., Hädicke, E., Hingmann, R., Schmidt, F. & Lindner, P. 1992 Rheological and small angle neutron scattering investigation of shear-induced particle structures of concentrated polymer dispersions submitted to plane Poiseuille and Couette flow. *J. Rheol.* **36**, 743–787.

Laun, H. M., Bung, R. & Schmidt, F. 1991 Rheology of extremely shear thickening polymer dispersions (passively viscosity switching fluids). *J. Rheol.* **35**, 999–1034.

Metzner, A. B. & Whitlock, M. 1958 Flow behavior of concentrated (dilatant) suspensions. *Trans. Soc. Rheol.* **11**, 239–254.

Phung, T. N., Brady, J. F. & Bossis, G. 1996 Stokesian dynamics simulation of Brownian suspensions. *J. Fluid Mech.* **313**, 181–207.

Russel, W. B., Saville, D. A. & Schowalter, W. R. 1989 *Colloidal Dispersions*. Cambridge University Press.

Strivens, T. A. 1976 The shear thickening effect in concentrated dispersion systems. *J. Colloid Interface Sci.* **57**, 476–487.

Willey, S. J. & Macosko, C. W. 1978 Steady shear rheological behavior of PVC plastisols. *J. Rheol.* **22**, 525–545.

Wolfram, S. 1991 *Mathematica: A System for Doing Mathematics by Computer*. Addison-Wesley.